Accepted Manuscript

Magnetic SiO$_2$@CoFe$_2$O$_4$ nanoparticles decorated on graphene oxide as efficient adsorbents for the removal of anionic pollutants from water

Chella Santhosh, Ehsan Daneshvar, Pratap Kollu, Sirpa Peräniemi, Andrews Nirmala Grace, Amit Bhatnagar

Please cite this article as: C. Santhosh, E. Daneshvar, P. Kollu, S. Peräniemi, A.N. Grace, A. Bhatnagar, Magnetic SiO$_2$@CoFe$_2$O$_4$ nanoparticles decorated on graphene oxide as efficient adsorbents for the removal of anionic pollutants from water, *Chemical Engineering Journal* (2017), doi: http://dx.doi.org/10.1016/j.cej.2017.03.144

Magnetic SiO$_2$@CoFe$_2$O$_4$ nanoparticles decorated on graphene oxide as efficient adsorbents for the removal of anionic pollutants from water

Chella Santhosh [a,*], Ehsan Daneshvar [a], Pratap Kollu [b,c], Sirpa Peräniemi [d],

Andrews Nirmala Grace [e], Amit Bhatnagar [a,*]

[a] *Department of Environmental and Biological Sciences, University of Eastern Finland,*

P.O. Box 1627, FI-70211, Kuopio, Finland

[b] *School of Physics, University of Hyderabad, Gachibowli, Hyderabad- 500046, India*

[c] *Newton Alumnus Researcher- The Royal Society London, Thin Film Magnetism group, Cavendish Laboratory, University of Cambridge, Cambridge CB3 0HE, UK*

[d] *School of Pharmacy, University of Eastern Finland, P.O. Box 1627, FI-70211, Kuopio, Finland*

[e] *Center for Nanotechnology Research, VIT University, Vellore-632014, Tamil Nadu, India*

*Corresponding authors: Tel. +358 503696419: E-mail: santhosh.chella@uef.fi;
amit.bhatnagar@uef.fi;

Abstract

In this study, magnetic nanocomposites viz. $SiO_2@CoFe_2O_4$ nanoparticles decorated on graphene oxide were synthesized using solvothermal and sol-gel processes. The prepared nanocomposite materials were used as magnetic adsorbents for the removal of organic and inorganic pollutants (acid black 1 dye and Cr(VI) ions as model pollutants) from aqueous solution. The structure, morphology and other physico-chemical properties of nanocomposites were characterized by X-ray diffraction (XRD), field emission-scanning electron microscopy (FE-SEM), high resolution-transmission electron microscopy (HR-TEM), vibrating sample magnetometer (VSM), X-ray Photo spectroscopy (XPS), zeta potential and Fourier infrared (FT-IR) spectroscopy. Batch mode adsorption studies were conducted with the prepared nanocomposites to determine the maximum adsorption capacity of acid black 1 dye and Cr(VI) ions as a function of contact time, pH, adsorbent dosage and initial adsorbate concentrations. Different kinetic and isotherm models were tested to describe and elucidate the adsorption mechanisms. Based on the experimental results obtained, the synthesized materials proved to exhibit considerable potential for the removal of acid black 1 and Cr(VI) ions from aqueous solution.

Keywords: Silica nanoparticles; cobalt ferrites; graphene oxide; dyes; metal ions.

1. Introduction

Synthetic organic dyes and metals are important aquatic pollutants which are present in effluents of many industries e.g. paper, textile, printing, leather, mining, food and cosmetics etc. [1, 2]. Various dyes are toxic and hard to biodegrade, when they are discharged directly to the water streams. In addition to that, most of the dyes are highly visible in water which affects the transparency of water, resulting in the reduction of direct light penetration and oxygen gas solubility in water. Approximately, more than 7×10^5 ton dyes are discharged to the environment per annum [3]. Currently, one of the world's major problem is to treat the highly-colored dye effluents, before discharge them to the environment.

Besides dyes (organic pollutants), various inorganic pollutants, such as metal ions are also one of the crucial aquatic pollutants which are dangerous to both living organisms and the environment, due to their bioaccumulation and biomagnification properties [4-6]. Chromium is one of such toxic metals which poses serious risk to the environment and human beings. The + 3 and + 6 oxidation states are the most commonly observed in chromium compounds. Hexavalent chromium, Cr(VI) is known to be five hundred times more toxic than the trivalent one (Cr(III)). Maximum allowable concentration of Cr(VI) in surface water has limited to 0.05 mg/L by World Health Organization (WHO) [7]. Thus, there is an urgent need for the removal of dyes and Cr(VI) from water and wastewater using an effective and robust technique [8-10]. Various technologies have been developed to remove the organic and inorganic pollutants from water and wastewater such as ion exchange, photocatalytic degradation, chemical treatment, membrane process, electrochemical process and adsorption [11-15]. Among these techniques, adsorption is one of the most favorable processes for the removal of organic and inorganic pollutants because of its easy operation, cost-effectiveness, simple design and high adsorption capacity towards toxic pollutants.

Various adsorbents, such as activated carbon, nanoparticles, biomaterials and metal oxides have

been extensively applied for the removal of organic and inorganic pollutants from water and wastewater [16-20]. Among the various adsorbents, graphene oxide (GO) is one of the derivative of carbon family, which can be easily synthesized from the natural graphite using modified hummer's method. Graphene oxide contains more oxygen groups (such as -OH, -COOH, -O- and C=O) and has abundant other functional groups [21], which help for higher adsorption of organic and inorganic pollutants [22-25], due to increased number of active sites on their surface [26]. Hence, more research is focused on using GO and their composites towards the removal of various pollutants [27, 28]. There is easy stacking between layers due to π-π bonding between the GO layers while using for practical application. However, separation of GO from aqueous solution requires high energy centrifugation and separation techniques [29]. Hence, to overcome these drawbacks, functionalization of GO is one of the efficient way to increase the adsorption capacity of various pollutants [30, 31]. To separate easily from the aqueous solution, magnetic nanoparticles are widely used as composite materials, attached with GO sheets, which can act as a magnetically recoverable adsorbent. Among the various magnetic materials, cobalt ferrite ($CoFe_2O_4$) nanoparticles have gained much attention, due to their high corrosive stability and moderate magnetic saturation, easy and rapid separation [32-34]. However, bare magnetic nanoparticles will aggregate to larger nanoparticles with fewer activating groups and will dissolve easily in acidic medium. The biocompatible materials are stable in suspension and ecofriendly. Among various materials, SiO_2 is a biocompatible material [35, 36] which can effectively protect the magnetic nanoparticles, due to its stability under the acidic conditions.

Present work focuses on the preparation of GO decorated $SiO_2@CoFe_2O_4$ nanoparticles by solvothermal process followed by sol-gel process. The synthesized nanocomposites were further functionalized with 3-aminopropyltrimethoxysilane (APTMS) to attach the functional groups (e.g. NH_2). Furthermore, the synthesized nanocomposites were tested for their potential for the removal of organic (Acid black 1 dye) and inorganic (Cr (VI)) pollutants. The physical and chemical

properties of prepared nanocomposite were characterized and discussed in detail. The adsorption of pollutants onto the ternary nanocomposites was investigated by varying different operational parameters such as contact time, solution pH, adsorbent dosage and initial adsorbate concentration. The adsorption mechanisms were examined by various kinetic and isotherm models.

2. Experimental

2.1 Materials

Cobalt chloride ($CoCl_2.6H_2O$), ferric chloride ($FeCl_3.6H_2O$), sodium acetate, polyethylene glycol, and ethylene glycol were purchased from Sigma Aldrich, Finland. Tetraethyl orthosilicate (TEOS), 3-aminopropyltriethoxysilane (APTES), 2-propanol, ammonium hydroxide and toluene were purchased from Alfa asar, Finland. Graphite powder, sodium nitrate ($NaNO_3$), potassium permanganate ($KMnO_4$) and hydrogen peroxide (H_2O_2) (30%) were supplied by S.D.Fine Chem. Ltd, Mumbai, India. All the samples were prepared from Milli-Q water.

2.2. Preparation of $CoFe_2O_4$ nanoparticles

Cobalt ferrite ($CoFe_2O_4$) nanoparticles were synthesized by using solvothermal process, as reported in our previous publication [37]. In short, 150 mL of ethylene glycol was taken in a 250 mL conical flask, which contained ferric chloride and cobalt chloride. Then suspension was kept for ultrasonication for 2 h. Later, 3 g of polyethylene glycol and 10 g of sodium acetate were added to the mixture and kept for stirring for 30 min. Then the mixture was transferred to the Teflon sealed autoclave at 200°C for 10 h. Finally, the mixture was collected by external magnetic field, washed with water and ethanol several times, and then kept for drying in vacuum oven at 45°C overnight.

2.3. Preparation of graphene oxide

Graphene oxide (GO) was synthesized by using natural graphite as a precursor material, using modified Hummer's method. The detailed synthesis procedure was reported and discussed in our previous publication [37].

2.4. Synthesis of $SiO_2@CoFe_2O_4$ nanocomposites

The obtained cobalt ferrite nanoparticles were then coated with silica (SiO_2) nanoparticles by sol-gel process [38]. In short, 0.6 g of $CoFe_2O_4$ nanoparticles were dispersed in 50 mL of 2-propanol and 15 mL of DI water, followed by ultrasonication for 1 h. Then, 4 mL of TEOS and 10 mL of NH_4OH were added to the above mixture under continuous stirring for 10 h at room temperature. Finally, the mixture was washed with ethanol and DI water for several times and kept for drying in a vacuum oven at 45°C overnight.

2.5. Synthesis of amino-functionalized $SiO_2@CoFe_2O_4$ onto GO nanocomposite

The obtained $SiO_2@CoFe_2O_4$ nanocomposites were then functionalized with amino groups by adding APTES as a precursor material [39]. Herein, 0.5 g of $SiO_2@CoFe_2O_4$ nanocomposites were added to the 50 mL of toluene, followed by adding 4 mL of APTES. Then the solution was transferred to the reflux setup at 80 °C for 10 h under nitrogen atmosphere. Finally, the product was separated by external magnetic field using magnet and washed with DI water and ethanol for several times. The obtained product was then dispersed in 100 mL DI water and 100 mg of GO was added and stirred for 2 h at room temperature. The obtained product was then washed several times with water and ethanol and dried at vacuum oven at 45 °C overnight. The pictorial representation of synthesis procedure of all three nanocomposites is shown in Fig. 1.

Figure 1

2.6. Batch adsorption studies

Analytical grade $K_2Cr_2O_7$ and Acid black 1 dye (AB 1) were used to prepare the Cr(VI) and AB 1 stock solutions. The adsorption of Cr(VI) and AB 1 from aqueous solution was carried out by batch mode process in polyethylene centrifuge tubes containing adsorbate solution and a desired amount of nanocomposite adsorbent. Various parameters, such as, contact time (0 – 180 min), initial metal ion and dye concentration (2.5-100 mg L^{-1}), adsorbent dosage (0.25-2.0 g L^{-1}), solution pH (1-10) and ionic strength (5-40 g L^{-1}) were studied. The pH of the suspension was adjusted by adding

negligible amount of 0.1 M HCl or NaOH solutions. During the experiments, other parameters were kept constant, while studying one parameter. After shaking for a predetermined time, the solid-liquid phases were separated by external magnetic force, followed by filtration using 0.42 µm cellulose nitrate membrane filters. The concentration of Cr(VI) in the liquid phase was measured by 1,5-diphenylcarbohydrazide method using UV-Visible spectrophotometer in the maximum absorbance wavelength of 540 nm [21, 40, 41]. The concentration of AB 1 dye in the liquid phase was measured by using UV-Visible spectrophotometer in the maximum absorbance wavelength of 620 nm.

2.7. Adsorption Studies

The removal efficiency of AB 1 and Cr(VI) ions onto the synthesized nanocomposites were calculated from the difference between the initial concentration (C_i) and the equilibrium concentration (C_e) of pollutants in the supernatant after filtration. The adsorption percentage and equilibrium capacity of both these pollutants were calculated by using following Eqs. (1 and 2):

$$Adsorption\ (\%) = \frac{C_i - C_e}{C_i} \times 100 \tag{1}$$

$$q_e = \frac{v(C_i - C_e)}{W} \tag{2}$$

where C_i and C_e are the initial and final adsorbate concentration (mg L^{-1}), respectively; q_e and C_e are equilibrium adsorption capacity (mg g^{-1}) and concentration (mg L^{-1}), respectively of the dye and metal ions at equilibrium; V is the volume of dye and metal ion solution (L) and W is the weight of adsorbent (g). Three types of nanocomposites, viz., $SiO_2@CoFe_2O_4$, $SiO_2@CoFe_2O_4$-NH_2 and amino-functionalized $SiO_2@CoFe_2O_4$-GO were synthesized. After preliminary testing with all these nanocomposites, amino-functionalized $SiO_2@CoFe_2O_4$-GO nanocomposite showed the highest adsorption capacity compared to the other two nanocomposites, therefore, all the adsorption studies were done on amino-functionalized $SiO_2@CoFe_2O_4$-GO nanocomposites.

2.8. Measurements and characterization

The crystalline structure of the synthesized nanocomposites was identified by using a Rigaku Miniflex powder X-ray Diffraction (XRD) (Cu Kα = 1.5406 Å) over 2θ range from 10-80° C. The morphology of the composites was obtained with FE-SEM, (JSM-7600F). The samples were then characterized with High Resolution Transmission Electron Microscope (HR-TEM) (model: FEI-Technai G2, F30) operated at 300 kV to know the shape and size of the nanocomposites. The concentration of metal ions and dye in the solution was analyzed using UV-Visible spectroscopy (UV - 4200). The porous nature of the samples was investigated using physical adsorption of nitrogen on ASAP 2020 Micrometrics instrument. Prior to measurements, the samples were outgassed at 40°C with a heating rate of 10°C min^{-1} for 1 h. VSM analysis of the synthesized materials was carried out with Lake Shore Model (7410-S) under applied magnetic field at room temperature and FT-IR analysis was performed with Bruker, Germany (3000 Hyperion Microscope with vertex 80 FTIR system). X-ray Photo Spectroscopy (XPS) analysis was carried out by using a Thermo Scientific Multilab 2000 spectrometer with Mg source. Elemental analysis was performed with the CHNOS Vario EL cube analysis. Using S2 Picofox Total Reflection X-Ray Fluorescence spectrometer (TXRF, Bruker), the concentration of Co and Fe was analyzed in the supernatant after adding Ga (TraceCERT, Fluka) as an internal standard. Zeta potential was measured using Delsa nano C particle analyzer (Beckman Coulter, Inc.).

3. Results and discussion

3.1. XRD analysis

The crystalline phase and structure of nanocomposites were characterized with X-ray diffraction. Fig. 2 shows the XRD patterns of $SiO_2@CoFe_2O_4$, $SiO_2@CoFe_2O_4$-NH_2 and amino functionalized $SiO_2@CoFe_2O_4$–GO nanocomposites. The diffraction peaks at 2θ values of all three

nanocomposites at 18.40°, 30.39°, 35.61°, 43.37°, 53.82°, 57.19°, 62.75° and 74.38° were observed, which indexed to the crystal planes of (111), (220), (311), (400), (422), (511), (440) and (533), respectively. All the diffraction peaks of all three nanocomposites are assigned to the spinel-type $CoFe_2O_4$ in accordance with the standard JCPDS No. 22-1086. There is a broad peak in between 20 - 28°, which is represented as star in Fig. 2, is found in all the three nanocomposites, indicating the presence of SiO_2 coated on the $CoFe_2O_4$ nanoparticles [42, 43]. The GO sheets were exfoliated and got decorated with $SiO_2@CoFe_2O_4$ nanoparticles. This process might have led to the disappearance of the diffraction peaks of graphene oxide (001) in accordance with the earlier reports [43]. Thus, the three nanocomposites showed spinel structure having Oh7-Fd3m space group.

Figure 2

3.2. Morphological analysis

Fig. 3 shows the typical surface morphology and particle size of the synthesized nanocomposites which were analyzed by FE-SEM and HR-TEM. From the FE-SEM images, it is observed that the $CoFe_2O_4$ nanoparticles were distributed as homogeneous coated on SiO_2 nanoparticles and well decorated on GO sheets. Though the particles were homogenous with the estimated cluster size ranging between 100-150 nm of $CoFe_2O_4$ nanoparticles they were aggregated as seen from the FE-SEM images and SiO_2 nanoparticles were ranging in between 450-500 nm. HR-TEM images of amino functionalized $SiO_2@CoFe_2O_4$-GO are shown in Fig. 4. As seen from the images, the SiO_2 nanoparticles diameter were varied from 450-500 nm and the $CoFe_2O_4$ nanoparticles were the aggregation of a great number of smaller nanoparticles with an average size of 10-15 nm and exhibits porous structure. $SiO_2@CoFe_2O_4$ spheres were decorated on flake like graphene oxide nanosheets. Hence, it could be confirmed from the above analysis that the SiO_2 coated $CoFe_2O_4$ nanoparticles were homogeneously decorated on graphene oxide sheets.

Figure 3

Figure 4

3.3. Magnetic studies

The magnetic properties of synthesized nanocomposites were measured at room temperature at an applied magnetic field to the dependent magnetization. Fig. 5 shows the magnetic hysteresis loop of the synthesized $SiO_2@CoFe_2O_4$, $SiO_2@CoFe_2O_4\text{-}NH_2$ and amino-functionalized $SiO_2@CoFe_2O_4\text{-}GO$ respectively, which indicates that these three nanocomposites exhibit ferromagnetic nature. Fig. 5(a) shows the saturation magnetization of $SiO_2@CoFe_2O_4$ are estimated to be 28.5 emu g^{-1}. A similar behavior for $SiO_2@CoFe_2O_4\text{-}NH_2$ and amino-functionalized $SiO_2@CoFe_2O_4\text{-}GO$ is also observed, with less magnetization due to the attachment of nonmagnetic groups such as SiO_2, NH_2 and GO (Fig. 5(b, c)). However, the magnetic properties of $SiO_2@CoFe_2O_4\text{-}NH_2$ and amino-functionalized $SiO_2@CoFe_2O_4\text{-}GO$ is still enough, it can be easily separated from the aqueous solution, shown in Fig. 5 (Inset). When the applied magnetic field was removed, the nanocomposites were well dispersed in the aqueous solution after shaking for 1 min. This shows the excellent magnetic stability and redispersability, which can be used as efficient adsorbents for their practical applications with low external magnetic field.

Figure 5

3.4. Stability (or) solubility of adsorbents under acidic conditions

The solubility (or) stability of adsorbent is one of the important factors which should be considered for water treatment applications. There are only a few studies describing the stability of various adsorbents. In one study, authors examined the leaching of spinel ferrites and ICP-MS revealed that a negligible (<10 µg L^{-1}) amount of metal was leached [44]. In another study, the authors conducted the leaching test for Co-MPTS and pure cobalt ferrite at different pH conditions viz. pH 1.0-6.5. A significant leaching of Co and Fe was noticed from the pure cobalt ferrite however, the stability was

significantly increased for Co-MPTS after surface modification [45]. In another study, leaching tests were conducted with different magnetic materials ($MnFe_2O_4$, $CoFe_2O_4$ and Fe_3O_4) at different pH conditions. It was reported that 5 mg L^{-1} of metals were leached in the pH range of 3-11, while < 1 mg L^{-1} at above pH 6 [46].

In this study, the solubility (or) stability of the prepared materials was examined at low pH conditions (pH 1-3). Three synthesized adsorbents viz. $SiO_2@CoFe_2O_4$, $SiO_2@CoFe_2O_4-NH_2$ and Amino functionalized $SiO_2@CoFe_2O_4-GO$ were compared with bare $CoFe_2O_4$ (adsorbent dose: 0.5 g L^{-1}), were shaken with three pH solutions (pH 1, 2 and 3) for 180 min at room temperature. After that, adsorbents were separated from the solution by magnetic field and the supernatant was collected for analysis. Using Total Reflection X-Ray Fluorescence (TXRF) and Ga as standard, the concentration of Co and Fe was analyzed in the supernatant. Table 1 shows the results of dissolution of prepared materials under low pH conditions. As seen from the Table 1, higher dissolution of bare $CoFe_2O_4$ nanoparticles was observed as compared to composites. In the case of $SiO_2@CoFe_2O_4-NH_2$ composites, a significant control on leaching of Co and Fe was noticed, which is due to the coating of SiO_2 and amino-functionalization groups on the surface of $CoFe_2O_4$ nanoparticles. Furthermore, in case of amino-functionalized $SiO_2@CoFe_2O_4-GO$, the leaching of Co and Fe was further decreased due to the addition of graphene oxide nanosheets to the composite. These results confirm that leaching of Co and Fe can be significantly reduced in nanocomposites under acidic pH conditions (pH 1-3) as compared to bare cobalt ferrite nanoparticles. However, as noticed, some leaching of Co and Fe was recorded even from the composites at lower pH conditions, which can be explained by the fact that the surface of $CoFe_2O_4$ nanoparticles was not completely covered with amino-functionalization and SiO_2 nanoparticles. Vatta et al. [47] have also reported that the stability of magnetite particles in strong acidic solutions was improved by 87% when the surface was coated with diethyeleamine-functionalized silica. In this study, the stability of

$CoFe_2O_4$ (Co and Fe) in strong acidic solutions was improved by 93% and 98%, respectively when the surface was coated with SiO_2, amino functionalization and GO sheets.

Table 1

3.5. FT-IR analysis

Fourier transform infrared (FTIR) analyses of $SiO_2@CoFe_2O_4$, $SiO_2@CoFe_2O_4-NH_2$ and amino functionalized $SiO_2@CoFe_2O_4-GO$ were performed in the range of 400-4000 cm^{-1}. Fig. 6 show the peaks of 928 and 588 cm^{-1} are ascribed to Co-O and Fe-O vibrations of $CoFe_2O_4$, respectively. The characteristic peaks at 1102, 798 and 461 cm^{-1} were ascribed to the typical symmetric and bending vibrations of Si-O-Si [48, 49], respectively. The wide peaks at 3390, 1562 and 1635 cm^{-1} in all the three nanocomposites corresponds to the stretching vibration and bending vibrations of O-H groups, which are on the surface of the $CoFe_2O_4$ nanoparticles as well as absorbed water molecules. Compared with Fig. 6(a), the characteristic peaks at 3421 and 1542 cm^{-1} were ascribed to stretching and bending vibrations of N-H groups respectively, which can clearly see from Fig. 6 (b,c). The characteristic peaks at 2918 and 2850 cm^{-1} are ascribed to the asymmetric and symmetric stretching of the CH_2 groups of APTES [50] respectively. These results show that the SiO_2 and $CoFe_2O_4$ nanoparticles were likely to be coated with amino groups.

Figure 6

3.6. XPS analysis

XPS measurement was recorded to explore the elemental composition of synthesized nanocomposites. The binding energy obtained in the XPS analysis was corrected for specimen charging by referencing the C 1s peak to 284.6 eV. Fig. 7 shows the XPS wide scan survey of (a) $SiO_2@CoFe_2O_4$, (b) $SiO_2@CoFe_2O_4-NH_2$ and (c) amino-functionalized $SiO_2@CoFe_2O_4-GO$ nanocomposites. Fig. 7(a) show the distinct peaks due to C 1s, O 1s, Co 2p, Fe 2p and Si 2p are evident in the wide scan XPS survey of $SiO_2@CoFe_2O_4$. In Fig. 7(b), the distinct peaks due to C1s,

O1s, Fe2p, Co2p, Si 2p and N1s are evident in the wide scan XPS survey of $SiO_2@CoFe_2O_4-NH_2$. Whereas Fig. 7(c) shows the distinct peaks due to C1s, O1s, Fe2P, Co2p, Si2p and N1s are evident in the wide scan XPS survey of amino functionalized $SiO_2@CoFe_2O_4-GO$. The inset tables show the elemental composition of the materials. Hence, the prepared nanocomposites don't have impurities and proves that the materials were synthesized well with the solvothermal and sol-gel process. The peaks obtained at 284.6, 530, 780, 710 and 101 eV correspond to the C 1s in sp^2 carbon, O1s of adsorbed oxygen, Co 2p, Fe 2p and Si species. Fig. 8 shows the deconvoluted spectrum of element peaks in the amino-functionalized $SiO_2@CoFe_2O_4-GO$ nanocomposites. In the deconvoluted spectrum C1s spectrum of amino-functionalized $SiO_2@CoFe_2O_4-GO$, four Gaussian peaks were centered at 283.1, 284.6, 285.1 and 286.2 eV. The binding energy at 283.1 and 284.6 eV could be assigned to the graphite C and C-C bond (sp^2) of graphene respectively. Peak at 285.1 eV is ascribed to the C-O bond, while the other peak at 286.2 eV is assigned to the C=O bond, which is shown in Fig. 8(a) [51]. In Fig. 8(b), two peaks at 708.5 and 721.3 eV are attributed to the Fe 2p3/2 and Fe 2p1/2 of Fe^{3+} ions, which agrees with $CoFe_2O_4$ [52]. Two strong peaks at 780.1 and 795.9 eV for Co 2p3/2 and Co 2p1/2 were observed (Fig. 8(c)), indicating the oxidation state of Co^{2+} in $CoFe_2O_4$ [52]. Fig. 8(d) shows the O1s spectra can be ascribed to the peak at 530.1, which is characteristic of the lattice oxide oxygen of the metal oxides as Fe-O and Co-O of $CoFe_2O_4$.

Figure 7

Figure 8

3.7. Adsorption studies

3.7.1. Effect of adsorbent dosage

While conducting batch mode studies, adsorbent dosage is also considered as one of the important parameters. The effect of adsorbent dosage on the removal of AB 1 and Cr(VI) ions was studied by varying the adsorbent dosage concentration from 0.25 to 2.0 g L^{-1} (Fig. 9). The adsorption of AB 1

and Cr(VI) ions increased with an increase of adsorbent dosage, due to the large number of active

sites on the adsorbent surface available for adsorption and hence the removal of AB 1 and Cr(VI)

ions was increased. With a further increase, it led to saturation and this might be due to the non-

availability of the active sites at higher dosage. Hence, the maximum adsorption of dye and Cr(VI)

ions for synthesized nanocomposites was found at 1.5 and 2.0 g L^{-1} dose with 99.8% and 98% of

adsorption capacity, respectively.

Figure 9

3.7.2. Effect of solution pH

Solution pH is one of the important parameter in the adsorption process, which has direct influence

on the synthesized nanocomposites. The absorbance spectra was measured under different pH to

study the stability of the AB 1 dye and Cr(VI) and it did not shift at varied pH values. The pH

values were varied from 2 to 10 for AB 1 dye, and 1 to 10 for Cr(VI) ions for the synthesized

adsorbent. Fig. 10(a) depicts that the adsorption of AB 1 was higher in pH 2.0, which was decreased

by increasing the pH from 3.0 – 10.0. On the other hand, the adsorption of Cr(VI) ions was at pH

1.0 (Fig. 10(b)), which was decreased as the pH increased. It can be clearly seen from Fig. 10 that

the adsorption capacity was highly dependent on pH of the solution. Speciation of Cr(VI) ions is

strongly dependent on the solution pH. Basically, Cr(VI) ions exist in aqueous solution with the

predominant species of $HCrO_4^-$, CrO_4^{2-}, H_2CrO_4 and $Cr_2O_7^{2-}$, depending on the total chromium ions

concentration and pH of the solution. When the pH of the solution is acidic, $HCrO_4^-$ and $Cr_2O_7^{2-}$ are

the predominant species up to pH 5 [53], whereas CrO_4^{2-} is dominant at pH > 6.5 [54]. In case of

dye, AB 1 is first dissolved in aqueous solution, and the sulfonate groups dissociate and are

converted to anionic ions. At lower pH, surface sites become protonated and the adsorbent surface

becomes positively charged which helps to enhance the adsorption of negatively charged species

(AB 1 dye and Cr(VI) ions). On the other hand, adsorption of AB 1 and Cr(VI) was decreased with

increasing pH. This may be due to the competition for the active sites by OH⁻ ions and the electrostatic repulsion of negative species (AB 1 dye and Cr(VI)) ions by the negatively charged adsorbent surface at high pH. Similar results were also reported by other researchers where low pH was found favorable for AB 1 and Cr(VI)) ions [55, 56]. Therefore, under low pH conditions, the hydrogen bonds between $HCrO_4^-$ and functional groups (-NH_2^+ and Si-OH) on the adsorbent surface would play an important role in the adsorption process [57].

The zeta potential of an adsorbent plays a crucial role in the adsorption process. As can be seen from Fig 10(c), amino-functionalized $SiO_2@CoFe_2O_4$-GO possess a positive surface charge with pH of point of zero charge (pHpzc) = 5.9. It is well known that at pH < pzc (pH < 5.9), adsorption of anions is favorable. However, in the case of cations, the favorable adsorption condition is pH > pzc (pH > 5.9) [58]. Therefore, in an acidic environment (pH < pzc), a higher adsorption efficiency of anionic species is expected because of the electrostatic attraction forces between the positively charged adsorbent surface and negatively charged adsorbate.

Figure 10

3.7.3. Effect of contact time

The adsorption of AB 1 and Cr(VI) ions by amino-functionalized $SiO_2@CoFe_2O_4$-GO as a function of contact time was studied (Fig. 11). The adsorption of AB 1 and Cr(VI) ions was found to increase with time and after 2 h, equilibrium was achieved. Based on the obtained results, 140 min was selected as the equilibrium time for the rest of the experiments.

To know the mechanism of rate-controlling steps during the adsorption of AB 1 and Cr(VI) ions onto the nanocomposites, various kinetic models were simulated with the help of experimental data, by using non-linear forms of pseudo-first-order, pseudo-second-order and Avrami models (Eqs. 3-5) [59-61].

$$q_t = q_e\left(1 - e^{-k_1 t}\right) \qquad (3)$$

$$q_t = \frac{k_2 q_e^2 t}{1 + k_2 q_e t} \qquad (4)$$

$$q_t = q_e\left(1 - e^{\left(-(K_{AV} t)^n AV\right)}\right) \qquad (5)$$

where q_e and q_t (mg g^{-1}) are the uptake capacities of pollutant ions at equilibrium and at time t (min) respectively, k_1 (min^{-1}) and k_2 (g mg^{-1}min^{-1}) are the pseudo-first and pseudo-second-order rate constants, respectively. K_{AV} (min^{-1}) is the Avrami constant. The above models were fitted to the experimental data, and resulting plots are shown in Fig. 11 (a) and (b) for AB 1 and Cr(VI) ions, respectively on amino-functionalized SiO_2@$CoFe_2O_4$-GO nanocomposites.

Respective parameters for each model are summarized in Table 2. The theoretical q_e values of AB 1 and Cr(VI) ions were closer to the calculated experimental values with lower RMSE and high correlation coefficient (R^2) for the pseudo-second-order kinetic model. Thus, the above results show that pseudo-second-order kinetic model provides a better correlation as compared to pseudo-first-order and Avrami models for the adsorption of AB 1 and Cr(VI) ions onto the synthesized nanocomposites.

Figure 11

Table 2

The transport of adsorbate molecules from the aqueous solution to the surface of the adsorbent particles is followed by diffusion of the adsorbate molecules into the interior pores of the adsorbent, which is likely to be a slow process, and is therefore, considered as rate-determining step [62]. The use of Weber and Morris intra-particle diffusion model has been greatly explored to analyze the nature of the rate-controlling step which is represented by Eq. (6) to elucidate its mechanism [63]:

$$q_t = K_p t^{\frac{1}{2}} + I \qquad (6)$$

whereas K_p is the intra-particle diffusion constant (mg g^{-1} min$^{-1/2}$) and I (mg g^{-1}) is the intercept. According to intra-particle diffusion model, if adsorption of a solute is controlled by the intra-particle diffusion process, a plot of q_t versus $t^{1/2}$ should yield a straight line. The Weber and Morris plots of Cr(VI) and AB 1 dye adsorption on prepared nanocomposite are shown in Fig. 11 (c). It can be seen from the figure that there are two separate zones: first linear portion (phase I) and second linear part (phase II). In phase I, approximately 65% and 75% of rapid uptake of Cr(VI) and AB 1, respectively took place by nanocomposite within 120 min. This might be due to the immediate utilization of the most readily available binding sites on the adsorbent surface. Phase II represents a very slow diffusion of the adsorbate from the surface site into the inner pores. In this study, the intercept of the line fails to pass through the origin and the R^2 values are also less than 0.99. The deviation of straight line in Weber and Morris model might be due to difference in the rate of mass transfer in the initial and final stages of adsorption [64]. The values for rate parameters and R^2 for intra-particle diffusion model are calculated and listed in Table 2.

3.7.4. Adsorption isotherms

To determine the adsorption capacity of the synthesized nanocomposites, the equilibrium adsorption of AB 1 and Cr(VI) ions was studied as a function of pollutants concentration (C_i = 2.5-100 mg L^{-1}), and the results are shown in Fig. 12 (a and b). An adsorption capacity of 130.74 and 136.40 mg g^{-1} was achieved for AB 1 and Cr(VI) ions, respectively onto amino-functionalized SiO_2@$CoFe_2O_4$-GO nanocomposites at room temperature. As the concentration increased, active sites of amino functionalized SiO_2@$CoFe_2O_4$-GO nanocomposites become saturated and a plateau was reached after 2 h, indicating that no more sites are available for adsorption. It should be noted that the adsorption of pollutant ions increased quickly with time and then reached to equilibrium in 120 min. The adsorption was rapid in the beginning due to the availability of plenty of vacant sites on the adsorbent surface at an initial stage. As the duration increased, the available active sites

became unavailable for adsorption, resulting in decrease in driving force, lengthening of the equilibrium level and hence decreasing the adsorption rate.

In this work, two-parameter and three-parameter isotherm models were studied, such as Langmuir, Freundlich, Redlich–Peterson, and Sips isotherm models to describe the adsorption equilibrium data. The Langmuir isotherm is applicable for monolayer adsorption onto the homogeneous surface of an adsorbent [65]. The Freundlich isotherm is based on multilayer adsorption onto the heterogeneous surface of the adsorbent [66]. The Sips model is a combination of Langmuir and Freundlich models that has three parameters [67]. The Redlich-Peterson model incorporates three parameters and can be applied either in homogenous or heterogeneous systems [68]. The non-linear forms of Langmuir, Freundlich, Sips and Redlich-Peterson models are represented by the following equations (Eqs. 7-10).

$$q_e = \frac{q_m K_L C_e}{1 + K_L C_e} \tag{7}$$

$$q_e = K_F C_e^{\frac{1}{n}} \tag{8}$$

$$q_e = \frac{q_m (K_S C_e)^m}{1 + (K_S C_e)^m} \tag{9}$$

$$q_e = \frac{K_{RP} C_e}{1 + a_{RP} C_e^{\beta}} \tag{10}$$

where q_e (mg g^{-1}) is the amount of adsorbate adsorbed by the synthesized nanocomposites at equilibrium time and concentration; C_e is the equilibrium concentration at equilibrium time in solution (mg L^{-1}); q_m (mg g^{-1}) is the maximum adsorption capacity; k_L is the Langmuir constant (L mg^{-1}); K_F and n are the Freundlich equilibrium constants and exponent, respectively; K_S (L mg^{-1}) in Sips model is the affinity constant; K_{RP} (L g^{-1}) and a_{RP} (L mg^{-1}) are Redlich-Peterson constants. The results of isotherm modeling of AB 1 and Cr(VI) ions adsorption onto amino-functionalized SiO$_2$@CoFe$_2$O$_4$-GO nanocomposites are presented in Table 3 and Fig. 12 (a and b).

Overall, Langmuir model with the higher values of coefficient of determination (R^2) (0.997 and 0.995) and lower values of root mean square error (RMSE) showed a better fit for pollutant ions adsorption onto prepared nanocomposites as compared to the other models. The good fitting of Langmuir isotherm model to the experimental data indicated that AB 1 and Cr(VI) ions adsorption takes place on homogenous surface of the synthesized nanocomposites. The influence of adsorption isotherm shape can be used to examine whether the adsorption is favorable or not in terms of R_L, a dimensionless constant, which is defined by the Eq. (11) [69]:

$$R_L = \frac{1}{1 + K_L C_i} \qquad (11)$$

where K_L is the Langmuir constant and C_i is the initial concentration of adsorbate. If $R_L < 1$, adsorption is considered as favorable and if $R_L > 1$, adsorption is considered as unfavorable. Table 3 shows that the R_L value is between 0 and 1, which indicates that the adsorption is favorable for pollutants studied onto the synthesized nanocomposites. A comparison between various adsorbents (cited in the literature) and prepared nanocomposites (in this study) was done for the removal of AB 1 and Cr(VI) ions (Table 4) [39, 70-84]. As seen from the Table 4, the prepared adsorbent is more effective than the other reported ones.

Figure 12

Table 3

Table 4
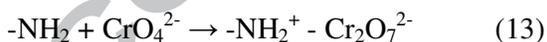
3.7.5. Effect of ionic strength

Industrial wastewater contains different types of suspended solids and salts. The existence of ions results in high ionic strength, which may affect the adsorption process [85]. In this study, the adsorption of Cr(VI) and AB 1 dye (with an initial concentration of 10 mg L^{-1}) was examined at different NaCl concentrations (0 - 40 g L^{-1}) (Fig. 13). In the case of Cr(VI) ions, the removal efficiency was found to decrease from 75 to 45 % by increasing the salt concentration (0 - 40 g L^{-1}).

This phenomenon might be explained due to the competition of chloride (Cl$^-$) ions with Cr(VI) species for the same binding sites [86], resulting in lower Cr(VI) adsorption. Whereas in the case of AB 1 dye, a slight effect of salt concentration on dye adsorption was observed. The removal efficiency was almost same at lower concentration of NaCl (5 - 10 g L^{-1}), however, when the salt concentration was increased from 20 to 40 g L^{-1}, a decrease in the adsorption of AB 1 was noticed. The ionic strength increases as NaCl concentration increases, thereby, increasing the Cl$^-$ ions in the solution. It may hinder the positive surface of the adsorbent, leading to the decrease in electrostatic attraction forces, therefore the adsorption rate is decreased for AB 1 dye. The obtained results are in agreement with previous literature [87, 88].

Figure 13

3.7.6. Adsorption mechanism

As confirmed by the pH studies, at highly strong acidic medium, Cr(VI) ions are bound with the positively charged surface of nanocomposites by electrostatic attractions between amino groups, $CoFe_2O_4$ and $HCrO_4^-$. Therefore, the possible adsorption mechanism of Cr(VI) ions onto the nanocomposites can be described as follows: the amino groups (-NH$_2$) were protonated at pH values below 5 and adsorbed negatively charged species, Cr(VI) ions (CrO_4^{2-}, $HCrO_4^-$ and $Cr_2O_7^{2-}$) via electrostatic attractions by the following reactions (Eqs. 12-14) [74]:

$$-NH_2 + HCrO_4^- \rightarrow -NH_2^+ - HCrO_4^- \qquad (12)$$

$$-NH_2 + CrO_4^{2-} \rightarrow -NH_2^+ - Cr_2O_7^{2-} \qquad (13)$$

$$-NH_2 + Cr_2O_7^{2-} \rightarrow -NH_2^+ - Cr_2O_7^{2-} \qquad (14)$$

In case of AB 1, dye is in anionic form which can be attracted towards the positively charged surface of NH$_2$ groups and $CoFe_2O_4$ on the surface of the nanocomposites. The conceptual adsorption mechanism of AB 1 and Cr(VI) ions onto the prepared nanocomposites is shown in Fig. 14(a, b).

Figure 14

As shown in Fig. 15 (FT-IR spectra of amino-functionalized $SiO_2@CoFe_2O_4$-GO before and after adsorption of Cr(VI) ions and AB 1 dye), the characteristic peaks were similar with little shift and decrease in the adsorption intensity after adsorption. The characteristic peaks were observed at 1066, 1608 and 3389 cm^{-1} before adsorption, however, peaks were slightly shifted to 1073, 1632 and 3393 cm^{-1} after adsorption of Cr(VI) ions with decrease in the intensity. In the case of AB 1 dye, peaks were slightly shifted to 1080, 1632 and 3389 cm^{-1} after adsorption of AB 1 ions with decrease in the intensity. The decrease in the adsorption intensity might be due to the interaction of functional groups during the adsorption process.

Figure 15

3.7.7. Desorption and regeneration studies

Desorption and regeneration studies of the synthesized adsorbents are of crucial importance when assessing their commercial applications. The adsorption of AB 1 and Cr(VI) ions was done as explained in batch mode adsorption (section 2.6). Fig. 16 shows the desorption efficiency of amino functionalized $SiO_2@CoFe_2O_4$-GO nanocomposites for the adsorption of AB 1 and Cr(VI) ions after five recycling's. For desorption, pollutant loaded nanocomposite (0.5 g L^{-1}) was shaken with 10 mL of 0.1 M NaOH as the desorbing agent at 80 rpm for 2 h at 25°C. The adsorbent was separated by magnet and the supernatant was filtered with 0.42 µm cellulose nitrate membrane filters. The obtained filtrate was analyzed for residual ion concentration using UV-visible spectrophotometer and the pollutant desorbed materials were used as regenerated adsorbents. The adsorption-desorption process was repeated up to five cycles to determine the reusability potential of adsorbents. It was found that for amino functionalized $SiO_2@CoFe_2O_4$-GO, the desorbing capacity of AB 1 was 92% up to five cycles, whereas for Cr(VI) ions, it was 65% for five cycles

(Fig. 16). The efficiency was almost retained during five repeated cycles. The above experiments indicated that the nanocomposites could be regenerated for practical use.

Figure 16

4. Conclusions

Novel silica based nanocomposites were synthesized successfully by solvothermal and sol-gel processes and further tested for the adsorption of AB 1 dye and Cr(VI) ions from aqueous solution. XRD, FE-SEM, HR-TEM, FT-IR, XPS and VSM shows the prepared nanocomposites were in good quality without any impurities with the adopted procedure. The experimental data fitted well to the Langmuir isotherm model. The monolayer adsorption capacity of AB 1 and Cr(VI) ions onto amino functionalized $SiO_2@CoFe_2O_4$-GO was found to be 130.74 and 136.40 mg g^{-1}, respectively. Adsorption was influenced by solution pH, which reached a maximum at pH 2 for AB 1 and pH 1 for Cr(VI). Further, kinetic study revealed that the process followed pseudo-second-order kinetic model for both pollutants. Desorption experiments revealed the stable reusable capacity of the adsorbent, thus making it a potential candidate for commercialization. Hence, the prepared nanocomposites could be used as efficient adsorbents for the removal of pollutants from aqueous solution.

References

[1] M.J. Ahmed, S.K. Dhedan, Equilibrium isotherms and kinetics modeling of methylene blue adsorption on agricultural wastes-based activated carbons, Fluid Phase Equilibria 317 (2012) 9-14.

[2] H. Wang, X. Yuan, Y. Wu, X. Chen, L. Leng, H. Wang, H. Li, G. Zeng, Facile synthesis of polypyrrole decorated reduced graphene oxide–Fe 3 O 4 magnetic composites and its application for the Cr (VI) removal, Chemical Engineering Journal 262 (2015) 597-606.

[3] G. Crini, Non-conventional low-cost adsorbents for dye removal: a review, Bioresource technology 97 (2006) 1061-1085.

[4] M. Avila, T. Burks, F. Akhtar, M. Göthelid, P.C. Lansåker, M.S. Toprak, M. Muhammed, A. Uheida, Surface functionalized nanofibers for the removal of chromium (VI) from aqueous solutions, Chemical engineering journal 245 (2014) 201-209.

[5] A.B. Albadarin, C. Mangwandi, H. Ala'a, G.M. Walker, S.J. Allen, M.N. Ahmad, Kinetic and thermodynamics of chromium ions adsorption onto low-cost dolomite adsorbent, Chemical Engineering Journal 179 (2012) 193-202.

[6] W. Qi, Y. Zhao, X. Zheng, M. Ji, Z. Zhang, Adsorption behavior and mechanism of Cr (VI) using Sakura waste from aqueous solution, Applied Surface Science 360 (2016) 470-476.

[7] World health organization guidelines for drinking water quality, 4th ed., World Health Organization, Geneva, 2011.

[8] J. Wang, C. Chen, Biosorbents for heavy metals removal and their future, Biotechnology advances 27 (2009) 195-226.

[9] P. Yin, Q. Xu, R. Qu, G. Zhao, Y. Sun, Adsorption of transition metal ions from aqueous solutions onto a novel silica gel matrix inorganic–organic composite material, Journal of hazardous materials 173 (2010) 710-716.

[10] G. Hota, B.R. Kumar, W. Ng, S. Ramakrishna, Fabrication and characterization of a boehmite nanoparticle impregnated electrospun fiber membrane for removal of metal ions, Journal of materials science 43 (2008) 212-217.

[11] C.K. Ahn, D. Park, S.H. Woo, J.M. Park, Removal of cationic heavy metal from aqueous solution by activated carbon impregnated with anionic surfactants, Journal of hazardous materials 164 (2009) 1130-1136.

[12] Y. Zhao, D. Zhao, C. Chen, X. Wang, Enhanced photo-reduction and removal of Cr (VI) on reduced graphene oxide decorated with TiO 2 nanoparticles, Journal of colloid and interface science 405 (2013) 211-217.

[13] C. Hachem, F. Bocquillon, O. Zahraa, M. Bouchy, Decolourization of textile industry wastewater by the photocatalytic degradation process, Dyes and Pigments 49 (2001) 117-125.

[14] C.-J. Cheng, T.-H. Lin, C.-P. Chen, K.-W. Juang, D.-Y. Lee, The effectiveness of ferrous iron and sodium dithionite for decreasing resin-extractable Cr (VI) in Cr (VI)-spiked alkaline soils, Journal of hazardous materials 164 (2009) 510-516.

[15] Y. Chen, H. Xu, S. Wang, L. Kang, Removal of Cr (VI) from water using polypyrrole/attapulgite core–shell nanocomposites: equilibrium, thermodynamics and kinetics, RSC Advances 4 (2014) 17805-17811.

[16] R. Schneider, C. Cavalin, M. Barros, C. Tavares, Adsorption of chromium ions in activated carbon, Chemical Engineering Journal 132 (2007) 355-362.

[17] H. Yan, H. Wu, K. Li, Y. Wang, X. Tao, H. Yang, A. Li, R. Cheng, Influence of the surface structure of graphene oxide on the adsorption of aromatic organic compounds from water, ACS applied materials & interfaces 7 (2015) 6690-6697.

[18] M. Kousha, E. Daneshvar, H. Dopeikar, D. Taghavi, A. Bhatnagar, Box–Behnken design optimization of Acid Black 1 dye biosorption by different brown macroalgae, Chemical Engineering Journal 179 (2012) 158-168.

[19] E. Daneshvar, M. Kousha, M. Jokar, N. Koutahzadeh, E. Guibal, Acidic dye biosorption onto marine brown macroalgae: isotherms, kinetic and thermodynamic studies, Chemical engineering journal 204 (2012) 225-234.

[20] L. Ai, C. Zhang, Z. Chen, Removal of methylene blue from aqueous solution by a solvothermal-synthesized graphene/magnetite composite, Journal of hazardous materials 192 (2011) 1515-1524.

[21] C. He, Z. Yang, J. Ding, Y. Chen, X. Tong, Y. Li, Effective removal of Cr(VI) from aqueous solution by 3-aminopropyltriethoxysilane-functionalized graphene oxide, Colloids and Surfaces A: Physicochemical and Engineering Aspects 520 (2017) 448-458.

[22] G. Zhao, L. Jiang, Y. He, J. Li, H. Dong, X. Wang, W. Hu, Sulfonated graphene for persistent aromatic pollutant management, Advanced materials 23 (2011) 3959-3963.

[23] J. Wang, Z. Chen, B. Chen, Adsorption of polycyclic aromatic hydrocarbons by graphene and graphene oxide nanosheets, Environmental science & technology 48 (2014) 4817-4825.

[24] H. Wang, X. Yuan, G. Zeng, Y. Wu, Y. Liu, Q. Jiang, S. Gu, Three dimensional graphene based materials: Synthesis and applications from energy storage and conversion to electrochemical sensor and environmental remediation, Advances in colloid and interface science 221 (2015) 41-59.

[25] H. Wang, X. Yuan, Y. Wu, H. Huang, G. Zeng, Y. Liu, X. Wang, N. Lin, Y. Qi, Adsorption characteristics and behaviors of graphene oxide for Zn (II) removal from aqueous solution, Applied Surface Science 279 (2013) 432-440.

[26] J. Li, C. Chen, R. Zhang, X. Wang, Reductive immobilization of Re (VII) by graphene modified nanoscale zero-valent iron particles using a plasma technique, Science China Chemistry 59 (2016) 150-158.

[27] H. Yan, X. Tao, Z. Yang, K. Li, H. Yang, A. Li, R. Cheng, Effects of the oxidation degree of graphene oxide on the adsorption of methylene blue, Journal of hazardous materials 268 (2014) 191-198.

[28] G. Zhao, J. Li, X. Ren, C. Chen, X. Wang, Few-layered graphene oxide nanosheets as superior sorbents for heavy metal ion pollution management, Environmental science & technology 45 (2011) 10454-10462.

[29] X. Deng, L. Lü, H. Li, F. Luo, The adsorption properties of Pb (II) and Cd (II) on functionalized graphene prepared by electrolysis method, Journal of hazardous materials 183 (2010) 923-930.

[30] C.J. Madadrang, H.Y. Kim, G. Gao, N. Wang, J. Zhu, H. Feng, M. Gorring, M.L. Kasner, S. Hou, Adsorption behavior of EDTA-graphene oxide for Pb (II) removal, ACS applied materials & interfaces 4 (2012) 1186-1193.

[31] Y. Shen, B. Chen, Sulfonated graphene nanosheets as a superb adsorbent for various environmental pollutants in water, Environmental science & technology 49 (2015) 7364-7372.

[32] G.V. Jacintho, A.G. Brolo, P. Corio, P.A. Suarez, J.C. Rubim, Structural investigation of MFe2O4 (M= Fe, Co) magnetic fluids, The Journal of Physical Chemistry C 113 (2009) 7684-7691.

[33] X. Ren, J. Shi, L. Tong, Q. Li, H. Yang, Magnetic and luminescence properties of the porous CoFe2O4@ Y2O3: Eu3+ nanocomposite with higher coercivity, Journal of nanoparticle research 15 (2013) 1738.

[34] J. Hu, I.M. Lo, G. Chen, Comparative study of various magnetic nanoparticles for Cr (VI) removal, Separation and Purification Technology 56 (2007) 249-256.

[35] C.-W. Lu, Y. Hung, J.-K. Hsiao, M. Yao, T.-H. Chung, Y.-S. Lin, S.-H. Wu, S.-C. Hsu, H.-M. Liu, C.-Y. Mou, Bifunctional magnetic silica nanoparticles for highly efficient human stem cell labeling, Nano letters 7 (2007) 149-154.

[36] M. Catauro, F. Bollino, F. Papale, M. Gallicchio, S. Pacifico, Influence of the polymer amount on bioactivity and biocompatibility of SiO 2/PEG hybrid materials synthesized by sol–gel technique, Materials Science and Engineering: C 48 (2015) 548-555.

[37] S. Chella, P. Kollu, E.V.P. Komarala, S. Doshi, M. Saranya, S. Felix, R. Ramachandran, P. Saravanan, V.L. Koneru, V. Venugopal, Solvothermal synthesis of MnFe 2 O 4-graphene composite—Investigation of its adsorption and antimicrobial properties, Applied Surface Science 327 (2015) 27-36.

[38] M. Yamaura, R. Camilo, L. Sampaio, M. Macedo, M. Nakamura, H. Toma, Preparation and characterization of (3-aminopropyl) triethoxysilane-coated magnetite nanoparticles, Journal of Magnetism and Magnetic Materials 279 (2004) 210-217.

[39] S. Yang, T. Zeng, Y. Li, J. Liu, Q. Chen, J. Zhou, Y. Ye, B. Tang, Preparation of graphene oxide decorated Fe 3 O 4@ SiO 2 nanocomposites with superior adsorption capacity and SERS detection for organic dyes, Journal of Nanomaterials 16 (2015) 337.

[40] H. Qi, S. Wang, H. Liu, Y. Gao, T. Wang, Y. Huang, Synthesis of an organic–inorganic polypyrrole/titanium (IV) biphosphate hybrid for Cr (VI) removal, Journal of Molecular Liquids 215 (2016) 402-409.

[41] D. Song, K. Pan, A. Tariq, A. Azizullah, F. Sun, Z. Li, Q. Xiong, Adsorptive Removal of Toxic Chromium from Waste-Water Using Wheat Straw and Eupatorium adenophorum, PloS one 11 (2016) e0167037.

[42] M. Shao, F. Ning, J. Zhao, M. Wei, D.G. Evans, X. Duan, Preparation of Fe3O4@ SiO2@ layered double hydroxide core–shell microspheres for magnetic separation of proteins, Journal of the American Chemical Society 134 (2012) 1071-1077.

[43] C. Ren, X. Ding, H. Fu, C. Meng, W. Li, H. Yang, Preparation of amino-functionalized CoFe 2 O 4@ SiO 2 magnetic nanocomposites for potential application in absorbing heavy metal ions, RSC Advances 6 (2016) 72479-72486.

[44] X. Bao, Z. Qiang, W. Ling, J.-H. Chang, Sonohydrothermal synthesis of MFe 2 O 4 magnetic nanoparticles for adsorptive removal of tetracyclines from water, Separation and Purification Technology 117 (2013) 104-110.

[45] A. Kraus, K. Jainae, F. Unob, N. Sukpirom, Synthesis of MPTS-modified cobalt ferrite nanoparticles and their adsorption properties in relation to Au (III), Journal of colloid and interface science 338 (2009) 359-365.

[46] S. Zhang, H. Niu, Y. Cai, X. Zhao, Y. Shi, Arsenite and arsenate adsorption on coprecipitated bimetal oxide magnetic nanomaterials: MnFe 2 O 4 and CoFe 2 O 4, Chemical engineering journal 158 (2010) 599-607.

[47] L.L. Vatta, J. Kramer, K.R. Koch, Diethylenetriamine functionalized silica coated magnetite nanoparticles for selective palladium ion extraction from aqueous solutions, Separation Science and Technology 42 (2007) 1985-2002.

[48] Q. Wang, W. Gao, Y. Liu, J. Yuan, Z. Xu, Q. Zeng, Y. Li, M. Schröder, Simultaneous adsorption of Cu (II) and SO 4 2− ions by a novel silica gel functionalized with a ditopic zwitterionic Schiff base ligand, Chemical Engineering Journal 250 (2014) 55-65.

[49] S. Lan, X. Wu, L. Li, M. Li, F. Guo, S. Gan, Synthesis and characterization of hyaluronic acid-supported magnetic microspheres for copper ions removal, Colloids and Surfaces A: Physicochemical and Engineering Aspects 425 (2013) 42-50.

[50] Q.S. Manuchehri, H. Bakhtiari, N. Assi, A Facile Microwave Method to Produce High Crystalline CoFe 2 O 4 Nano-particles, Int. J. Bio-Inorg. Hybd. Nanomat 2 (2013) 423-427.

[51] C. Santhosh, P. Kollu, S. Felix, V. Velmurugan, S.K. Jeong, A.N. Grace, CoFe 2 O 4 and NiFe 2 O 4@ graphene adsorbents for heavy metal ions–kinetic and thermodynamic analysis, RSC Advances 5 (2015) 28965-28972.

[52] Y. Fu, H. Chen, X. Sun, X. Wang, Combination of cobalt ferrite and graphene: high-performance and recyclable visible-light photocatalysis, Applied Catalysis B: Environmental 111 (2012) 280-287.

[53] D. Park, Y.-S. Yun, H.W. Lee, J.M. Park, Advanced kinetic model of the Cr (VI) removal by biomaterials at various pHs and temperatures, Bioresource technology 99 (2008) 1141-1147.

[54] V. Campos, P.M. Büchler, Removal of chromate from drinking water using powder carbon steel, Environmental Geology 47 (2005) 926-930.

[55] N. Koutahzadeh, E. Daneshvar, M. Kousha, M. Sohrabi, A. Bhatnagar, Biosorption of hexavalent chromium from aqueous solution by six brown macroalgae, Desalination and Water Treatment 51 (2013) 6021-6030.

[56] X. Peng, X. Hu, D. Fu, F.L.Y. Lam, Adsorption removal of acid black 1 from aqueous solution using ordered mesoporous carbon, Applied Surface Science 294 (2014) 71-80.

[57] S.H. Araghi, M.H. Entezari, M. Chamsaz, Modification of mesoporous silica magnetite nanoparticles by 3-aminopropyltriethoxysilane for the removal of Cr (VI) from aqueous solution, Microporous and Mesoporous Materials 218 (2015) 101-111.

[58] S. Ghorai, A. Sarkar, M. Raoufi, A.B. Panda, H. Schönherr, S. Pal, Enhanced removal of methylene blue and methyl violet dyes from aqueous solution using a nanocomposite of hydrolyzed polyacrylamide grafted xanthan gum and incorporated nanosilica, ACS applied materials & interfaces 6 (2014) 4766-4777.

[59] S. Lagergren, About the theory of so-called adsorption of soluble substances, (1898).

[60] Y.-S. Ho, G. McKay, Pseudo-second order model for sorption processes, Process biochemistry 34 (1999) 451-465.

[61] M. Avrami, Kinetics of phase change. I General theory, The Journal of Chemical Physics 7 (1939) 1103-1112.

[62] A. El Nemr, Potential of pomegranate husk carbon for Cr (VI) removal from wastewater: Kinetic and isotherm studies, Journal of Hazardous Materials 161 (2009) 132-141.

[63] W. Weber, J. Morris, Intraparticle diffusion during the sorption of surfactants onto activated carbon, J. Sanit. Eng. Div. Am. Soc. Civ. Eng 89 (1963) 53-61.

[64] K. Panday, G. Prasad, V. Singh, Mixed adsorbents for Cu (II) removal from aqueous solutions, Environmental Technology 7 (1986) 547-554.

[65] I. Langmuir, The adsorption of gases on plane surfaces of glass, mica and platinum, Journal of the American Chemical society 40 (1918) 1361-1403.

[66] H. Freundlich, Kolloidchemie, Akademischer Verlagsgesellschaft, Leipzig (1909).

[67] R. Sips, On the structure of a catalyst surface, The Journal of Chemical Physics 16 (1948) 490-495.

[68] O. Redlich, D.L. Peterson, A useful adsorption isotherm, Journal of Physical Chemistry 63 (1959) 1024-1024.

[69] S. Rajput, C.U. Pittman, D. Mohan, Magnetic magnetite (Fe 3 O 4) nanoparticle synthesis and applications for lead (Pb 2+) and chromium (Cr 6+) removal from water, Journal of colloid and interface science 468 (2016) 334-346.

[70] M. Liu, T. Wen, X. Wu, C. Chen, J. Hu, J. Li, X. Wang, Synthesis of porous Fe 3 O 4 hollow microspheres/graphene oxide composite for Cr (VI) removal, Dalton Transactions 42 (2013) 14710-14717.

[71] S. Babel, T.A. Kurniawan, Cr (VI) removal from synthetic wastewater using coconut shell charcoal and commercial activated carbon modified with oxidizing agents and/or chitosan, Chemosphere 54 (2004) 951-967.

[72] J. Hu, C. Chen, X. Zhu, X. Wang, Removal of chromium from aqueous solution by using oxidized multiwalled carbon nanotubes, Journal of hazardous materials 162 (2009) 1542-1550.

[73] X. Lv, X. Xue, G. Jiang, D. Wu, T. Sheng, H. Zhou, X. Xu, Nanoscale zero-valent iron (nZVI) assembled on magnetic Fe 3 O 4/graphene for chromium (VI) removal from aqueous solution, Journal of colloid and interface science 417 (2014) 51-59.

[74] D. Zhao, X. Gao, C. Wu, R. Xie, S. Feng, C. Chen, Facile preparation of amino functionalized graphene oxide decorated with Fe 3 O 4 nanoparticles for the adsorption of Cr (VI), Applied Surface Science 384 (2016) 1-9.

[75] R. Wu, J. Qu, Y. Chen, Magnetic powder MnO–Fe 2 O 3 composite—a novel material for the removal of azo-dye from water, Water research 39 (2005) 630-638.

[76] G.Z. Kyzas, N.A. Travlou, O. Kalogirou, E.A. Deliyanni, Magnetic graphene oxide: effect of preparation route on reactive black 5 adsorption, Materials 6 (2013) 1360-1376.

[77] A.A. Atia, A.M. Donia, W.A. Al-Amrani, Adsorption/desorption behavior of acid orange 10 on magnetic silica modified with amine groups, Chemical Engineering Journal 150 (2009) 55-62.

[78] Y. Jiang, F. Li, G. Ding, Y. Chen, Y. Liu, Y. Hong, P. Liu, X. Qi, L. Ni, Synthesis of a novel ionic liquid modified copolymer hydrogel and its rapid removal of Cr (VI) from aqueous solution, Journal of colloid and interface science 455 (2015) 125-133.

[79] R. Fang, W. He, H. Xue, W. Chen, Synthesis and characterization of a high-capacity cationic hydrogel adsorbent and its application in the removal of Acid Black 1 from aqueous solution, Reactive and Functional Polymers 102 (2016) 1-10.

[80] S.C. Tang, P. Wang, K. Yin, I.M. Lo, Synthesis and application of magnetic hydrogel for Cr (VI) removal from contaminated water, Environmental Engineering Science 27 (2010) 947-954.

[81] C. Shen, Y. Shen, Y. Wen, H. Wang, W. Liu, Fast and highly efficient removal of dyes under alkaline conditions using magnetic chitosan-Fe (III) hydrogel, Water research 45 (2011) 5200-5210.

[82] X. Sun, L. Yang, Q. Li, J. Zhao, X. Li, X. Wang, H. Liu, Amino-functionalized magnetic cellulose nanocomposite as adsorbent for removal of Cr (VI): synthesis and adsorption studies, Chemical Engineering Journal 241 (2014) 175-183.

[83] H.-Y. Zhu, Y.-Q. Fu, R. Jiang, J. Yao, L. Xiao, G.-M. Zeng, Novel magnetic chitosan/poly (vinyl alcohol) hydrogel beads: preparation, characterization and application for adsorption of dye from aqueous solution, Bioresource technology 105 (2012) 24-30.

[84] Z. Hou, W. Zhu, H. Song, P. Chen, S. Yao, The adsorption behavior and mechanism investigation of Cr (VI) ions removal by poly (2-(dimethylamino) ethyl methacrylate)/poly (ethyleneimine) gels, Journal of the Serbian Chemical Society 80 (2015) 889-902.

[85] X. Xu, B.-Y. Gao, X. Tan, Q.-Y. Yue, Q.-Q. Zhong, Q. Li, Characteristics of amine-crosslinked wheat straw and its adsorption mechanisms for phosphate and chromium (VI) removal from aqueous solution, Carbohydrate polymers 84 (2011) 1054-1060.

[86] T. Anirudhan, J. Nima, P. Divya, Adsorption of chromium (VI) from aqueous solutions by glycidylmethacrylate-grafted-densified cellulose with quaternary ammonium groups, Applied Surface Science 279 (2013) 441-449.

[87] S. Zhao, F. Zhou, L. Li, M. Cao, D. Zuo, H. Liu, Removal of anionic dyes from aqueous solutions by adsorption of chitosan-based semi-IPN hydrogel composites, Composites Part B: Engineering 43 (2012) 1570-1578.

[88] A. Aguedach, S. Brosillon, J. Morvan, E.K. Lhadi, Influence of ionic strength in the adsorption and during photocatalysis of reactive black 5 azo dye on TiO 2 coated on non woven paper with SiO 2 as a binder, Journal of hazardous materials 150 (2008) 250-256.
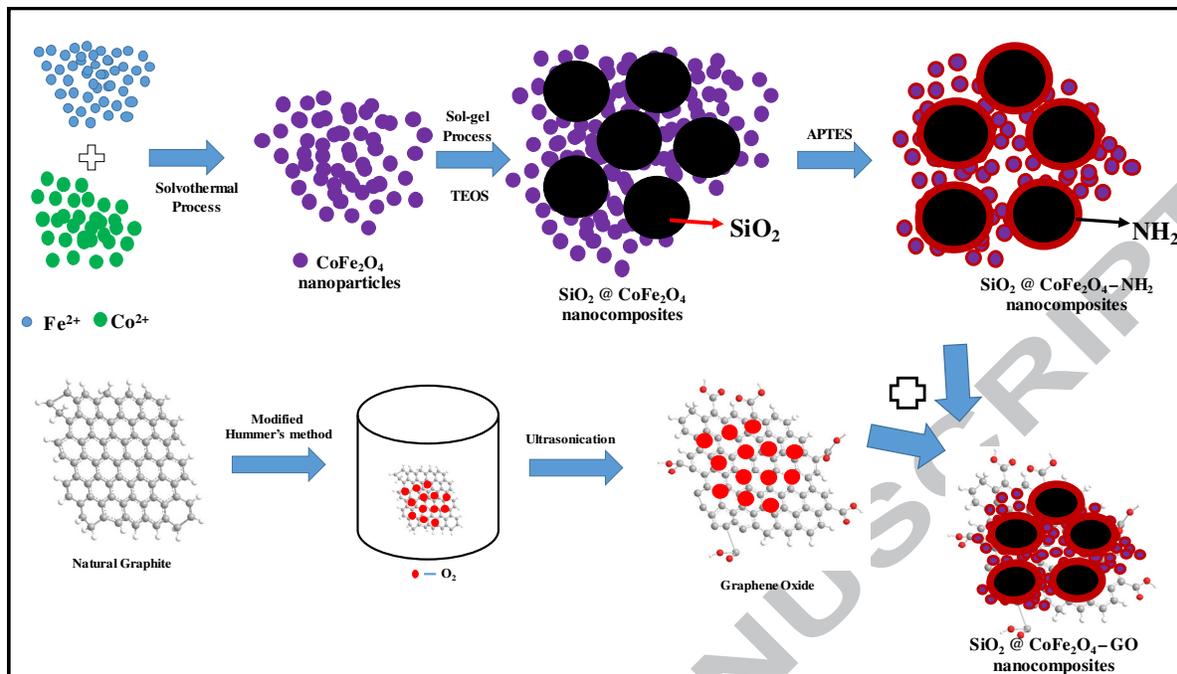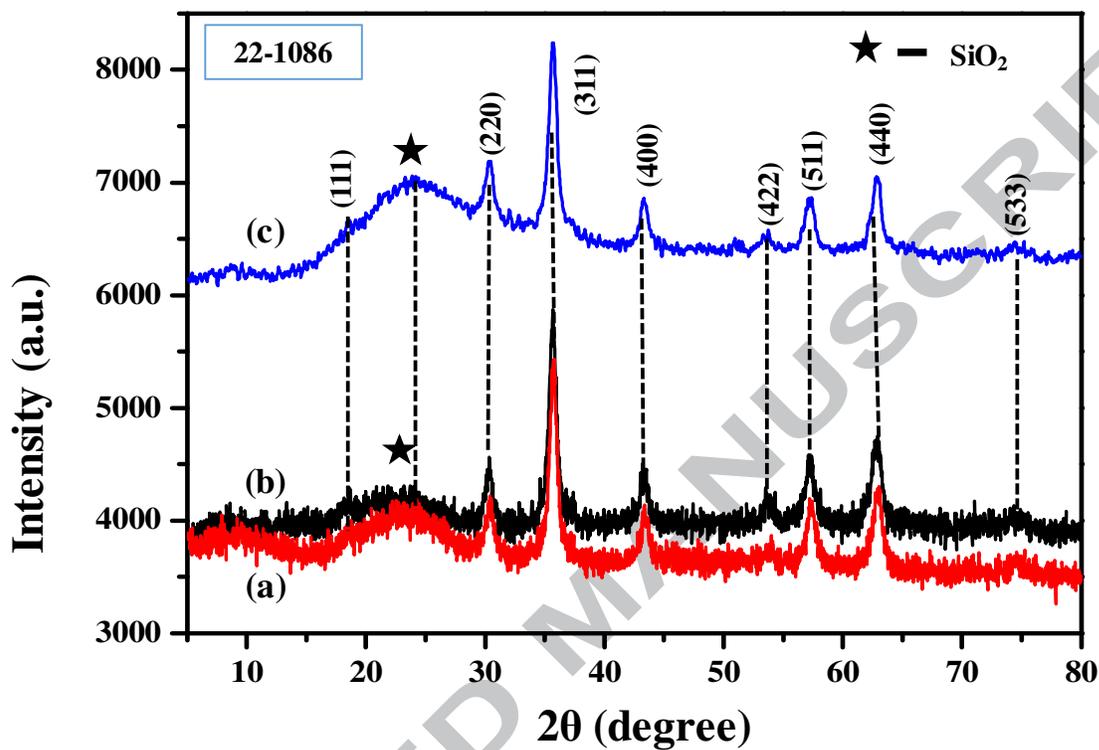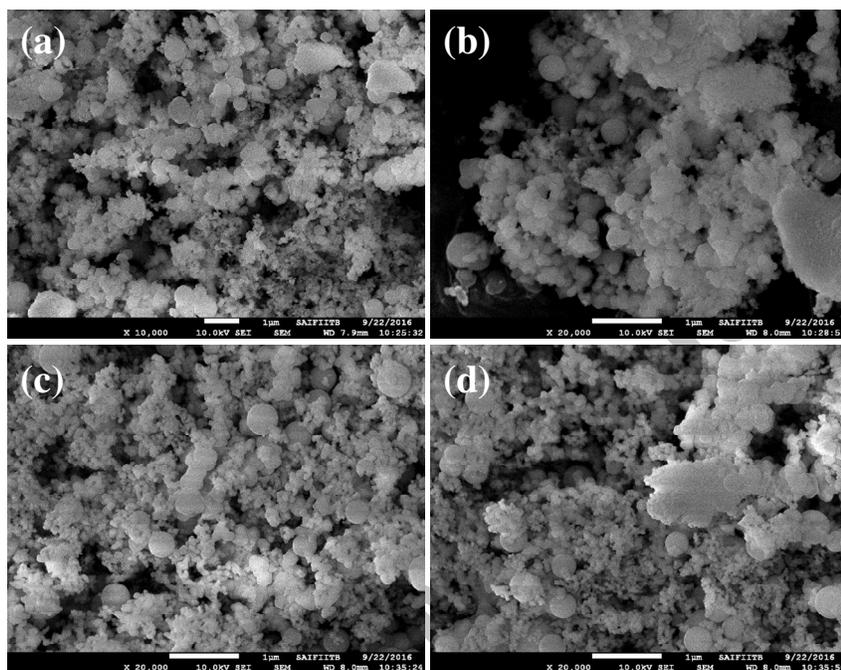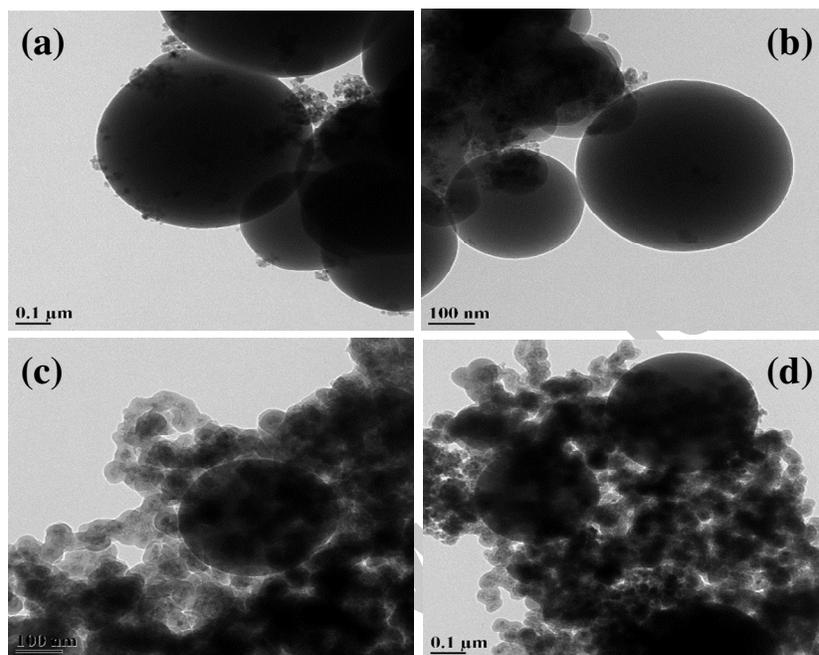
**Fig. 1.** Schematic representation of synthesis process for synthesized nanocomposites.

Fig. 2. XRD analysis of (a) $SiO_2@CoFe_2O_4$ (b) $SiO_2@CoFe_2O_4-NH_2$ and (c) amino-functionalized $SiO_2@CoFe_2O_4-GO$.
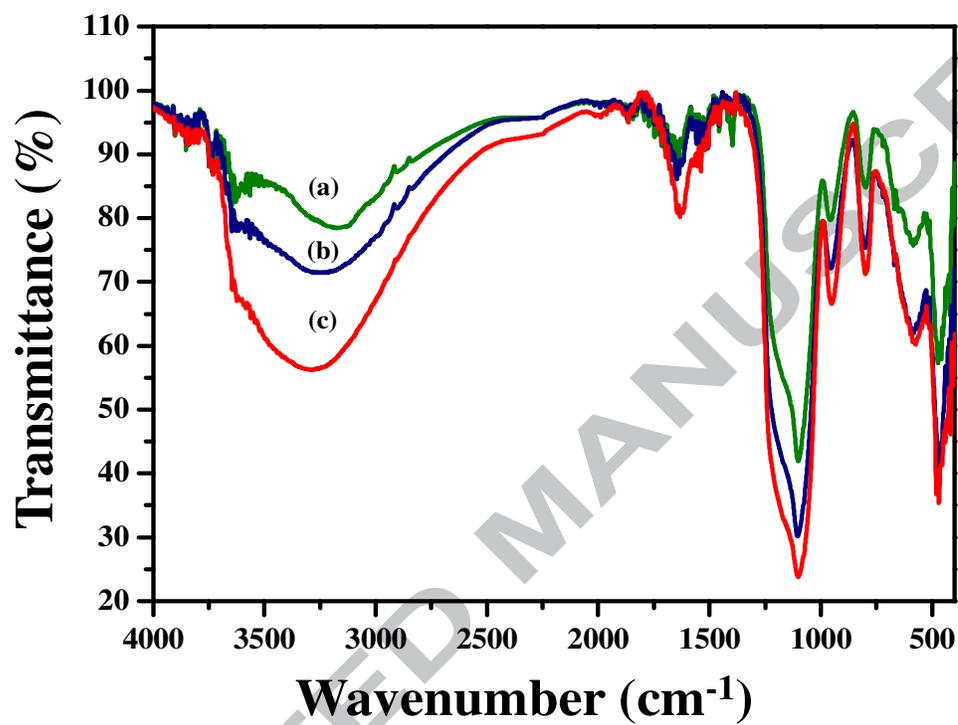
Fig. 3. FE-SEM images of (a) SiO_2@$CoFe_2O_4$, (b) SiO_2@$CoFe_2O_4$-NH_2,

(c-d) amino-functionalized SiO_2@$CoFe_2O_4$-GO.

Fig. 4. HR-TEM images of (a) $SiO_2@CoFe_2O_4$, (b) $SiO_2@CoFe_2O_4-NH_2$,

(c-d) amino-functionalized $SiO_2@CoFe_2O_4-GO$.
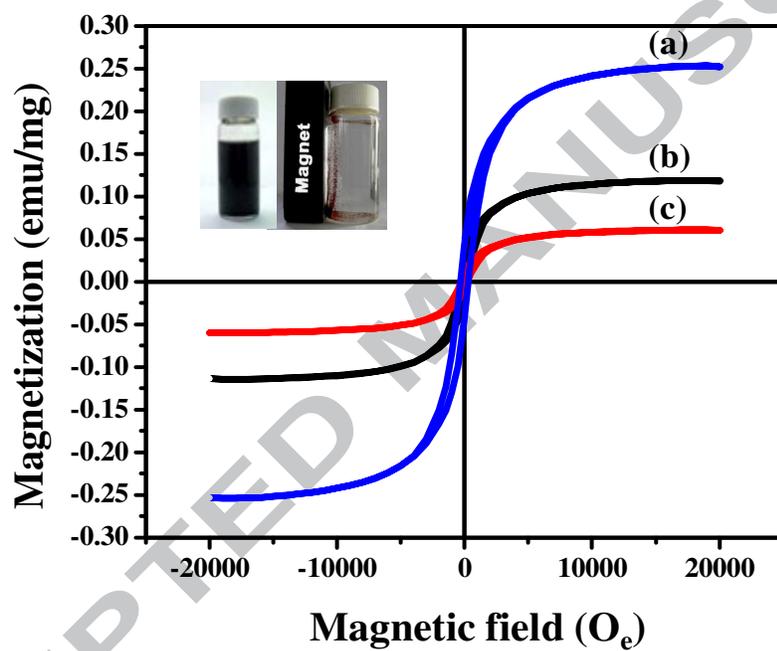
Fig. 5. Hysteresis (M-H) analysis of (a) $SiO_2@CoFe_2O_4$, (b) $SiO_2@CoFe_2O_4\text{-}NH_2$ and (c) amino - functionalized $SiO_2@CoFe_2O_4\text{–}GO$.

Fig. 6. FT-IR analysis of (a) $SiO_2@CoFe_2O_4$, (b) $SiO_2@CoFe_2O_4$-NH_2 and

(c) amino-functionalized $SiO_2@CoFe_2O_4$-GO.
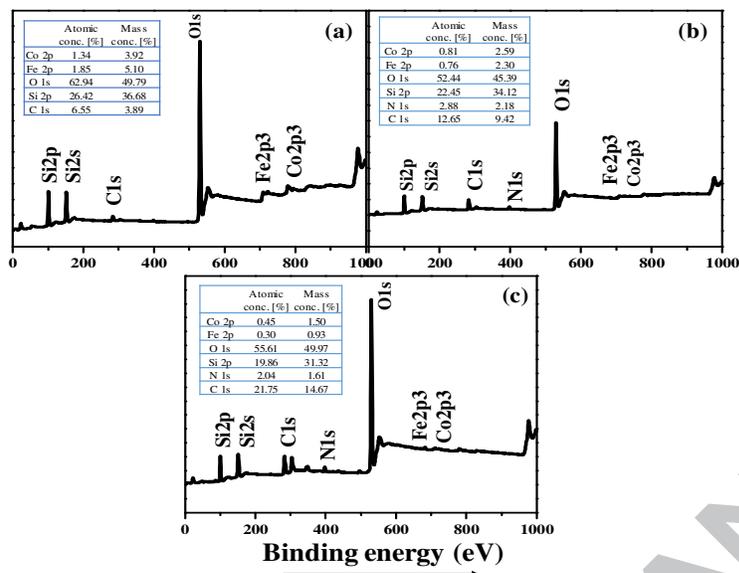
Fig. 7. Full scan XPS spectra of (a) $SiO_2@CoFe_2O_4$, (b) $SiO_2@CoFe_2O_4-NH_2$ and (c) amino -
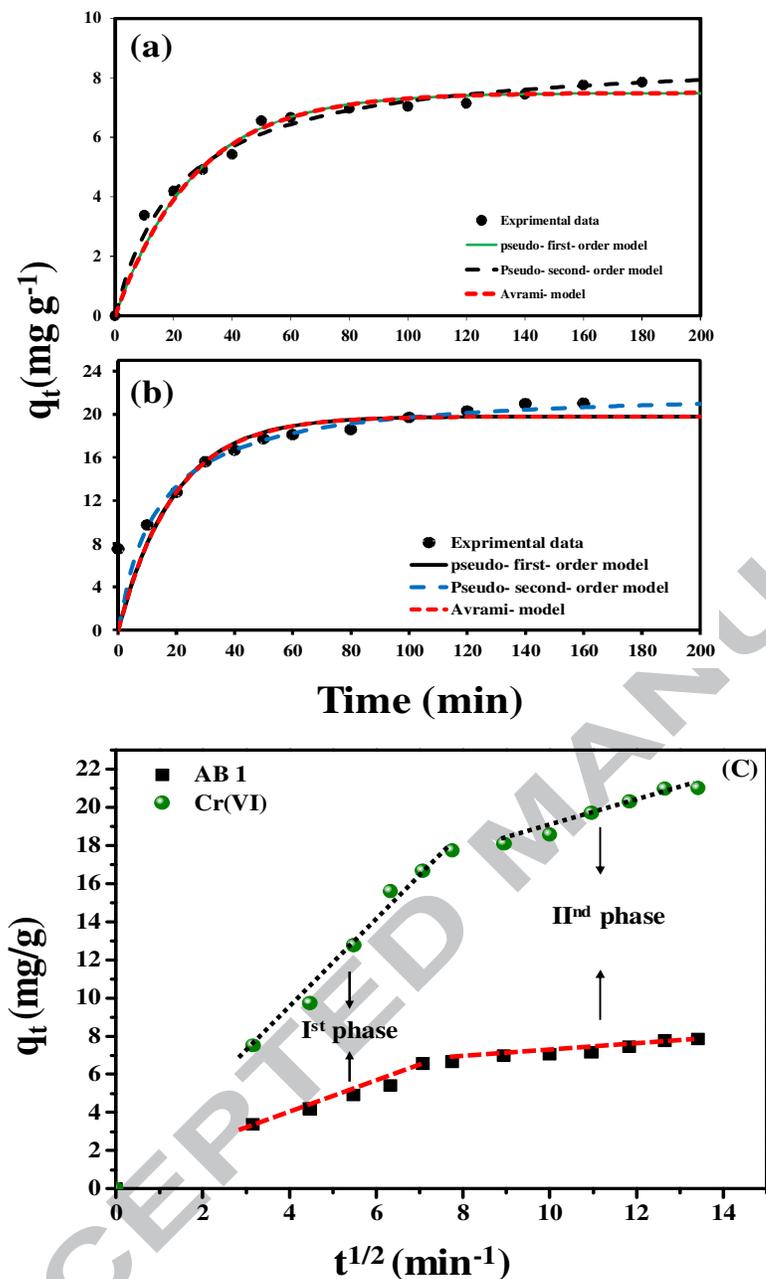
functionalized $SiO_2@CoFe_2O_4-GO$ nanocomposites.
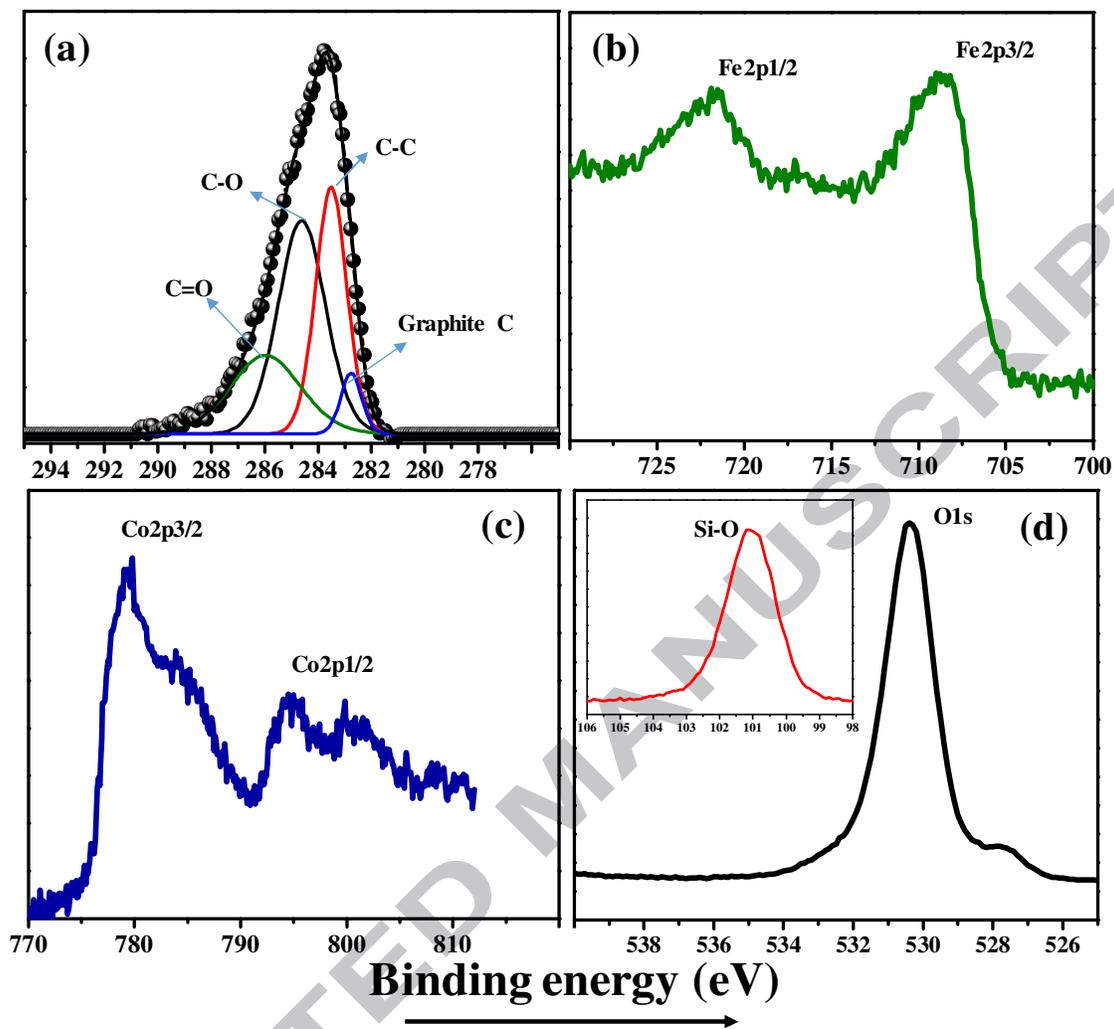
Fig. 8. XPS spectra of (a) C1s (b) Fe2p (c) Co2p and (d) O1s (Inset shows SiO_2) regions of amino-functionalized SiO_2@$CoFe_2O_4$-GO nanocomposites.
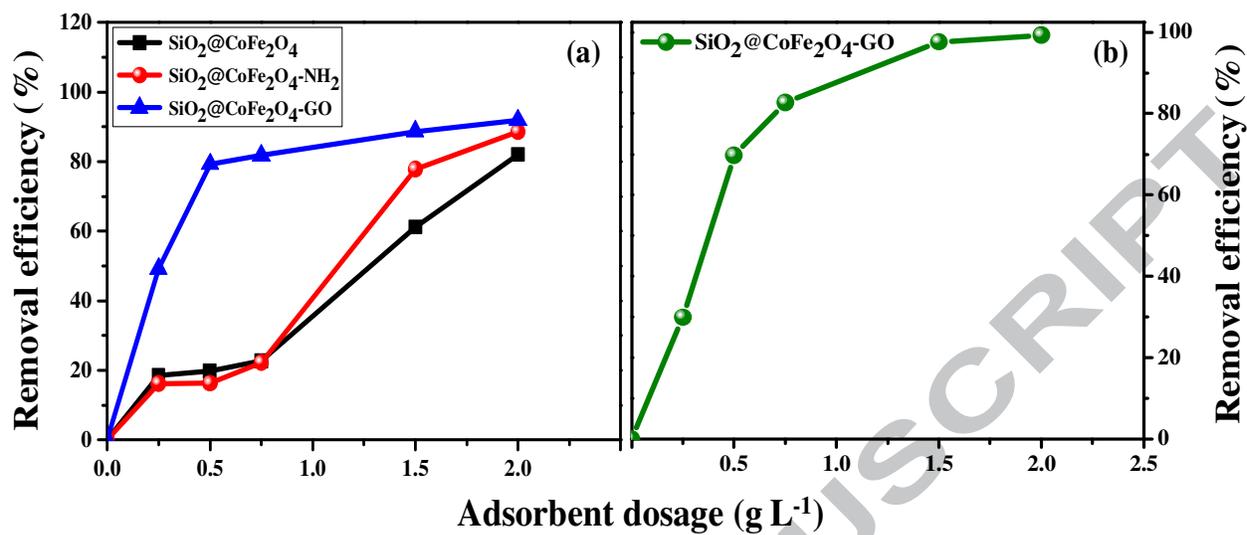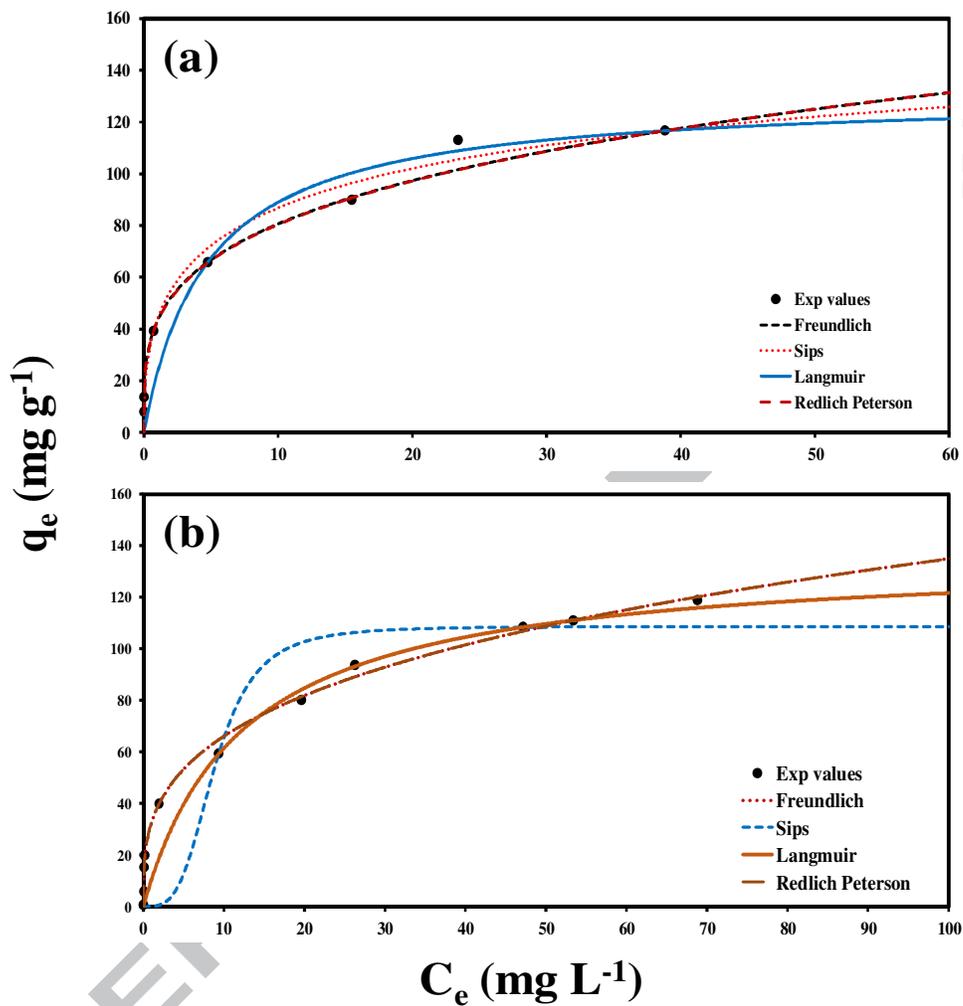
Fig. 9. Effect of adsorbent dosage on (a) AB 1 adsorption by synthesized nanocomposites, (b) Cr(VI) ions adsorption by amino-functionalized $SiO_2@CoFe_2O_4$-GO nanocomposites. (Contact time: 140 min, pH 1 for Cr(VI) ions and pH 2 for AB 1, initial concentration: 10 mg L^{-1}, temp: 25°C)
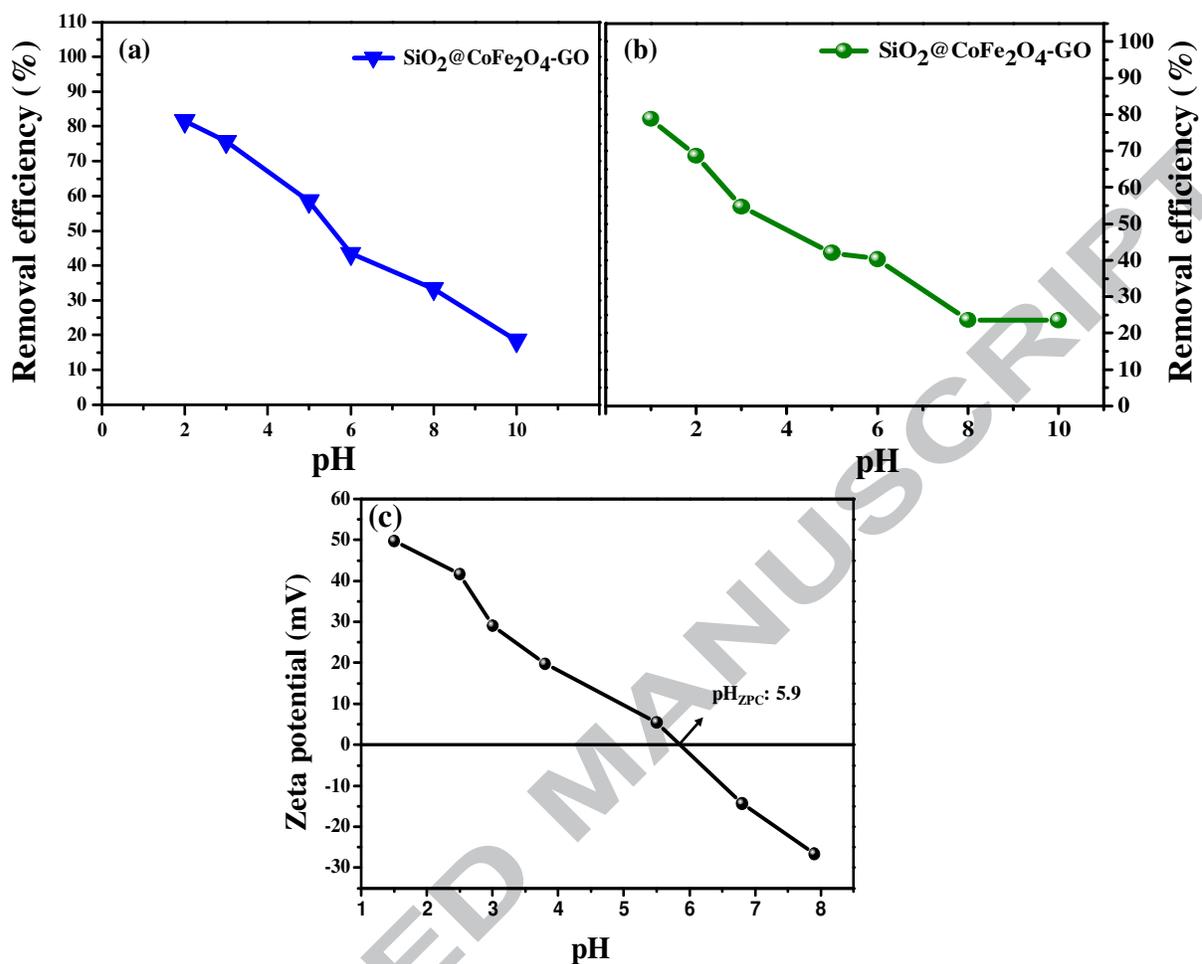
Fig. 10. Effect of (a) pH of AB 1, (b) pH of Cr(VI) ions adsorption (Contact time: 140 min, adsorbent dosage: 0.5 g L^{-1}, initial concentration: 10 mg L^{-1}, temp: 25°C), (c) Zeta potential of synthesized amino-functionalized SiO$_2$@CoFe$_2$O$_4$-GO.

Fig. 11. Kinetic studies of (a) AB 1 and (b) Cr(VI) adsorption by amino-functionalized

SiO$_2$@CoFe$_2$O$_4$-GO nanocomposites, fitting of different kinetic models to the experimental data

and Intra-particle diffusion model of AB 1 and Cr(VI) ions. (pH 1 for Cr(VI) ions and pH 2 for AB

1, adsorbent dosage: 0.5 g L^{-1}, initial concentration: 10 mg L^{-1}, temp: 25°C)

Fig. 12. Adsorption isotherms of (a) AB 1 and (b) Cr(VI) by amino-functionalized $SiO_2@CoFe_2O_4$-GO nanocomposites and fitting of different isotherm models to the experimental data. (Contact time: 140 min, pH 1 for Cr(VI) ions and pH 2 for AB 1, adsorbent dosage: 0.5 g L^{-1}, temp: 25°C)
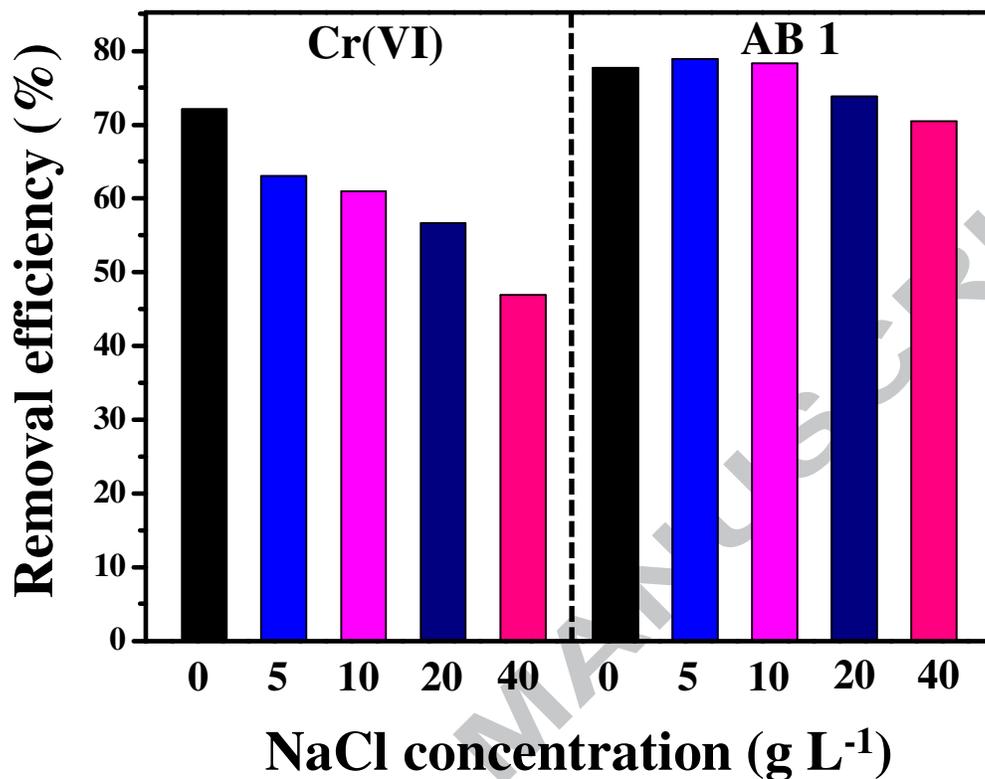
Fig. 13. Effect of ionic strength on the adsorption of Cr(VI) and AB 1 by prepared amino-functionalized $SiO_2@CoFe_2O_4$-GO. (pH 2 for AB 1 and pH 1 for Cr(VI) ions, contact time: 140 min, temperature: 25°C, adsorbent dosage: 0.5 g L-1, initial concentration: 10 mg L^{-1})
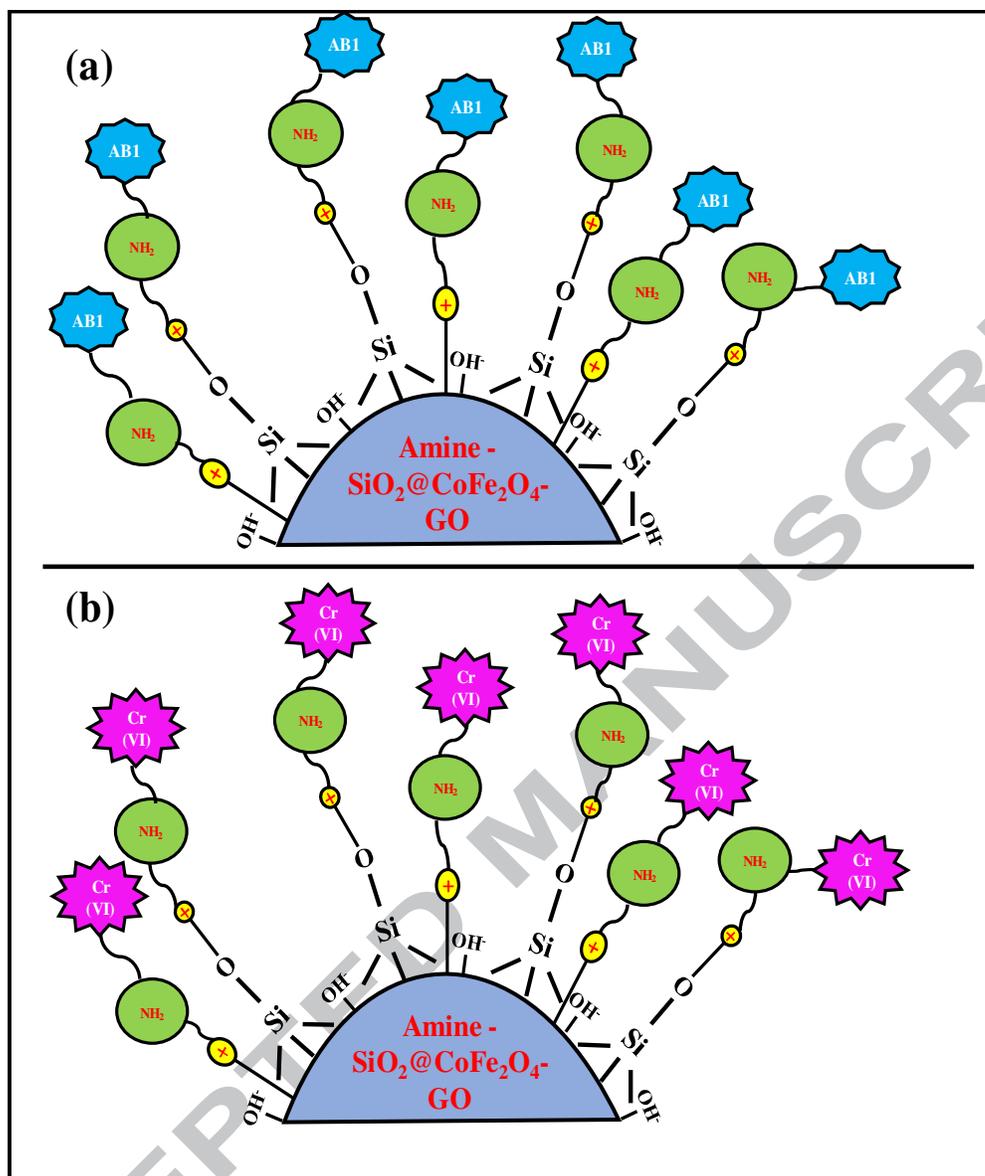
Fig. 14. Pictorial representation possible mechanism of amino-functionalized $SiO_2@CoFe_2O_4$-GO with AB 1 and Cr(VI).
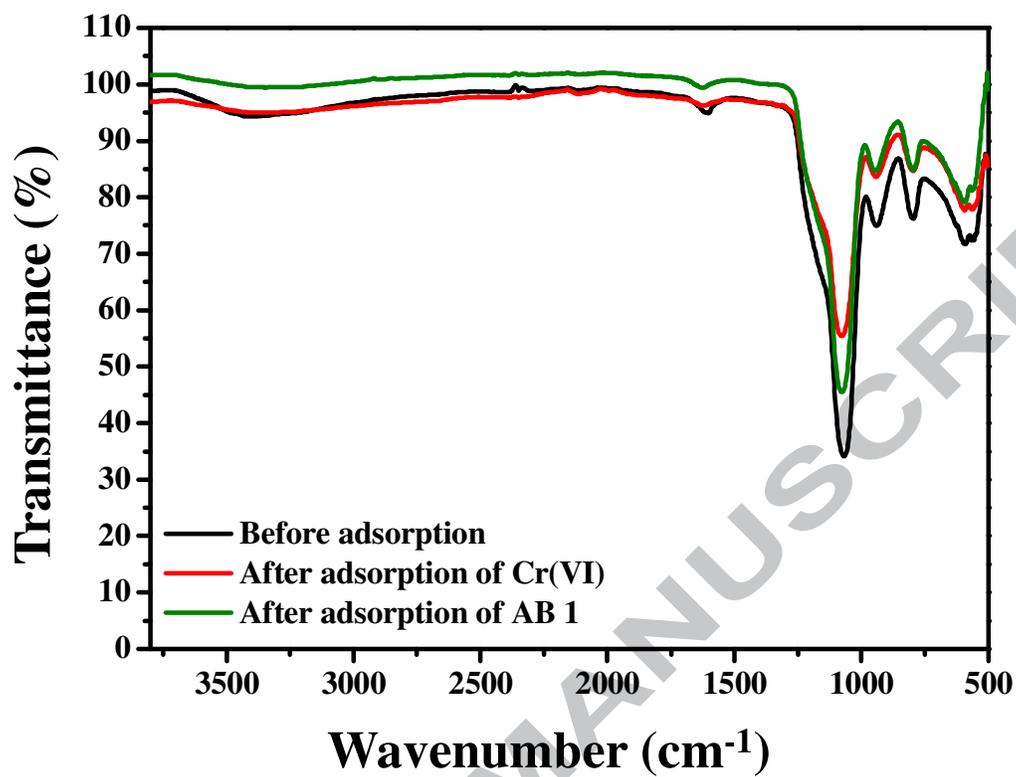
Fig. 15. FT-IR spectra of amino-functionalized $SiO_2@CoFe_2O_4$-GO before and after adsorption of Cr(VI) and AB 1 ions.
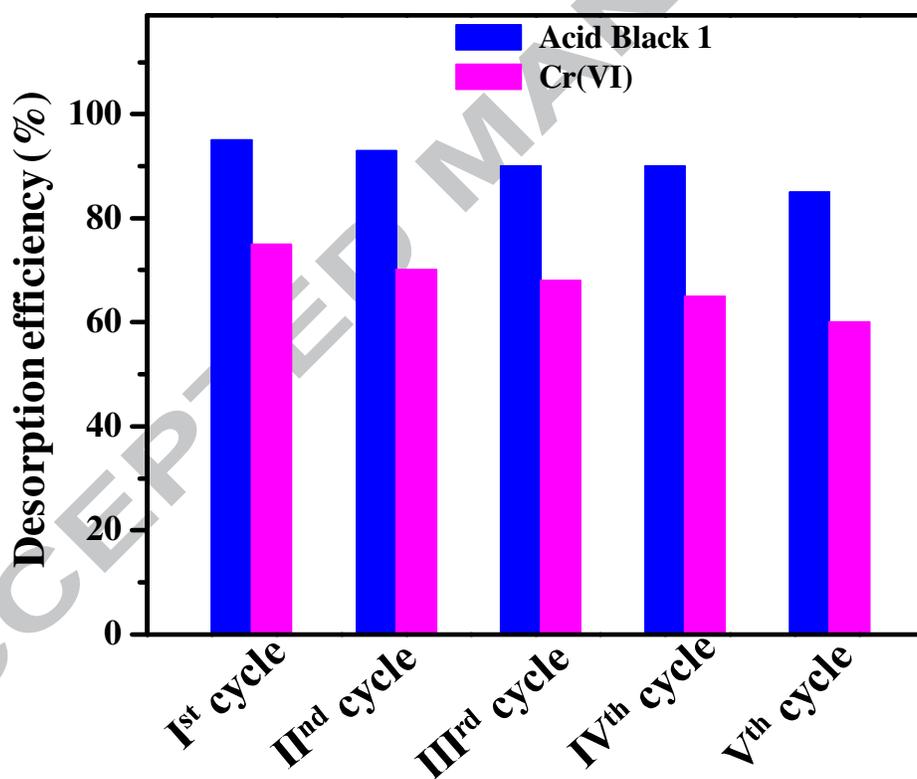
Fig. 16. Desorption studies of amino-functionalized SiO_2@$CoFe_2O_4$-GO with AB 1 and Cr(VI).

Table 1. Stability (or) solubility of adsorbents under acidic conditions.

Adsorbent	pH 1		pH 2		pH 3	
	Co (mg L^{-1})	Fe (mg L^{-1})	Co (mg L^{-1})	Fe (mg L^{-1})	Co (mg L^{-1})	Fe (mg L^{-1})
$CoFe_2O_4$	103.15	199.74	58.37	14.29	22.11	10.33
$SiO_2@CoFe_2O_4$-NH_2	8.95	5.41	5.10	2.65	3.59	1.27
Amino functionalized $SiO_2@CoFe_2O_4$-GO	7.52	4.09	6.98	2.10	5.22	0.701

Table 2. Kinetic parameters for acid black 1 and Cr(VI) ions onto the amino-functionalized SiO$_2$@CoFe$_2$O$_4$-GO nanocomposites.

Adsorbate	Pseudo-first-order model				
	q$_{e(exp)}$ (mg g^{-1})	k$_1$ (min^{-1})	q$_{e(cal)}$ (mg g^{-1})	RMSE	R^2
AB 1	7.85	0.03	7.49	0.34	0.974
Cr (VI)	21.01	0.05	19.79	5.51	0.813

Adsorbate	Pseudo-second-order model				
	q$_{e(exp)}$ (mg g^{-1})	k$_2$ (min^{-1})	q$_{e(cal)}$ (mg g^{-1})	RMSE	R^2
AB 1	7.85	0.005	8.80	0.24	0.998
Cr (VI)	21.01	0.003	22.39	4.72	0.992

Adsorbate	Avrami model					
	q$_{e(exp)}$ (mg g^{-1})	K$_{av}$	n$_{av}$	q$_{e(cal)}$ (mg g^{-1})	RMSE	R^2
AB 1	7.85	0.005	6.73	7.49	0.34	0.974
Cr (VI)	21.01	0.011	4.55	19.79	5.51	0.974

Adsorbate	Intra – particle diffusion model				
	C$_i$ (mg L^{-1})	I (mg g^{-1})	K$_p$ (mg g^{-1} min$^{-0.5}$)	RMSE	R^2
AB 1	10	2.15	0.45	1.33	0.964
Cr (VI)	10	0	2.13	8.17	0.944

Table 3. Isotherm studies for acid black 1 and Cr(VI) ions onto the amino-functionalized $SiO_2@CoFe_2O_4$-GO nanocomposites.

Adsorbent	Langmuir isotherm model			
	Amino-functionalized $SiO_2@CoFe_2O_4$-GO			
Pollutants	q_m (mg g^{-1})	K_L	R_L	R^2
AB 1	130.74	0.21	0.005	0.997
Cr (VI)	136.40	0.08	0.003	0.995

Adsorbent	Freundlich isotherm model			
	Amino-functionalized $SiO_2@CoFe_2O_4$-GO			
Pollutants	K_F	1/n	-	R^2
AB 1	43.04	0.27	-	0.786
Cr (VI)	32.27	0.31	-	0.510

Adsorbent	Sips isotherm model			
	Amino-functionalized $SiO_2@CoFe_2O_4$-GO			
Pollutants	q_m (mg g^{-1})	Ks(L mg^{-1})	n	R^2
AB 1	203.11	0.27	0.43	0.965
Cr (VI)	108.66	0.00045	3.52	0.976

Adsorbent	Redlich-Peterson isotherm model			
	Amino-functionalized $SiO_2@CoFe_2O_4$-GO			
Pollutants	K_{RP} (L mg^{-1})	q_{PR} (mg g^{-1})	n	R^2
AB 1	208.29	42.74	0.72	0.858
Cr (VI)	207.91	32.30	0.68	0.803

Table 4. Comparison of adsorption capacity of various adsorbents for acid black 1 and Cr(VI) removal with synthesized nanocomposites.

Adsorbent	q_m (mg/g)	Pollutant	pH	Ref.
Fe_3O_4/GO	32.33	Cr(VI)	4.5	[53]
Activated carbon	15.47	Cr(VI)	4.0	[54]
Oxidized MWCNTs	2.88	Cr(VI)	2.6	[55]
NZVI/Fe_3O_4/rGO	101.0	Cr(VI)	3.0	[56]
AMGO	123.4	Cr(VI)	2.0	[57]
Ionic liquid modified copolymer hydrogel	74.5	Cr(VI)	2.0	[78]
Amino-functionalized MSC composite	171.5	Cr(VI)	2.0	[82]
Magnetic hydrogel	205	Cr(VI)	-	[80]
poly(2-(dimethylamino)ethyl methacrylate)/poly(ethyleneimine) hydrogel composite	122.8	Cr(VI)	2.0	[84]
Amino-functionalized SiO_2@$CoFe_2O_4$-GO	136.40	Cr(VI)	1.0	*This study*
cationic hydrogel adsorbent	1771	AB 1		[79]
Magnetic chitosan-Fe(III) hydrogel	294.5	AR 73	12	[81]

Magnetic chitosan/poly(vinyl alcohol) hydrogel beads				
	470.1	CR	-	[83]
Magnetic powder MnO-Fe_2O_3	105.3	Acid red	3.5	[59]
Magnetic graphene oxide	164	Reactive Black 5	3	[60]
Monoamine modified magnetic silica	61.33	Acid orange 10	3	[61]
Amino-functionalized SiO_2@$CoFe_2O_4$-GO	130.74	Acid black 1	2	*This study*

Graphical Abstract
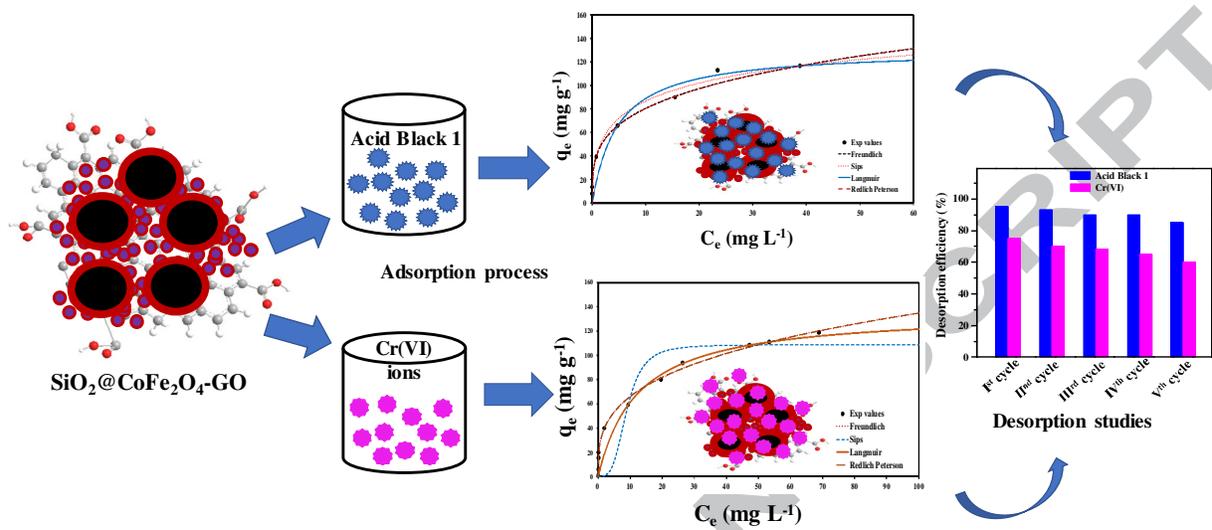
Highlights

➢ Novel magnetic $SiO_2@CoFe_2O_4$ -GO based nanocomposites were synthesized.

➢ Adsorption capacity for AB1 and Cr(VI) was found to be 130.74 and 136.40 mg g^{-1}.

➢ Desorption experiments revealed the stable reusable capacity of the nanocomposite.